Clim. Past, 22, 1085–1104, 2026
https://doi.org/10.5194/cp-22-1085-2026

Climate of the Past
Open Access
EGU

Glacial-interglacial shifts in dominant climate forcing over the last 33 ka in the northern South China Sea

Xueqin Zhao[1], Shengjie Ye[1], Jiahui Yao[1], Michael E. Meadows[2,3], Chengyu Weng[4], Yasong Wang[1], Mingxing Zhang[1], and Yunping Xu[1]

[1]Shanghai Frontiers Research Center of the Hadal Biosphere, College of Oceanography and Ecological Science, Shanghai Ocean University, Shanghai 201306, China
[2]School of Geography and Ocean Sciences, Nanjing University, Nanjing 210023, China
[3]Department of Environmental & Geographical Science, University of Cape Town, Cape Town 7701, South Africa
[4]State Key Laboratory of Marine Geology, Tongji University, Shanghai, China

Correspondence: Xueqin Zhao (xqzhao@shou.edu.cn)

Received: 22 December 2025 – Discussion started: 4 January 2026
Revised: 28 April 2026 – Accepted: 13 May 2026 – Published: 29 May 2026

Abstract. The northern South China Sea (SCS) is a critical region for understanding East Asian Monsoon dynamics. However, integrated, multi-proxy records elucidating long-term climatic and vegetation changes in this region remain fragmented, with a notable scarcity of coherent land-ocean interaction data during the Last Glacial Maximum (LGM). This gap has impeded progress in elucidating the mechanisms underpinning monsoon variability and in rigorously evaluating the performance of palaeoclimate models. To address this, we conducted a multi-proxy analysis combining palynological, organic- and inorganic-geochemical methods on a marine sediment core from the northern SCS to reconstruct environmental and oceanic dynamics at millennial-scale resolution that spans the last 33 ka. Our results reveal a clear contrast between glacial and interglacial regimes. The glacial period, especially the LGM, was characterized by higher sedimentation rates, elevated marine primary productivity, cooler and drier conditions, herb-dominated vegetation, and intensified fire activity. This regime was dominantly forced by low sea level and glacial aridity, which together promoted open terrestrial vegetation and enhanced nutrient input to the ocean. The deglaciation was characterized by pronounced warming, reduced productivity, increased moisture availability, a shift to pine-dominated vegetation, and reduced fire activity. A key finding is the ocean warming which began around 1.3 ka earlier than major terrestrial changes, indicating that tropical ocean-atmosphere interactions initiated the deglacial transition. The overall findings highlight a fundamental transition in climatic controls, from a glacial regime dominated by sea-level-driven shelf exposure and arid climate to an interglacial regime governed by tropical ocean-atmosphere dynamics. This study underscores the sensitivity of the northern SCS to both high- and low-latitude forcing and the value of integrated land-sea proxies in deciphering complex climate interactions.

1 Introduction

Low latitude regions play a critical role in the global climate and its dynamic because they are the seat of the most active moisture and heat exchanges between the atmosphere and the ocean expressed via the monsoon regime. Tropical and subtropical monsoon regions such as East Asia and the South China Sea (SCS) experience the most significant seasonal reversal in wind directions with associated migration of regional intense precipitation (Wang et al., 2017). Monsoon wind and precipitation patterns have changed significantly in the late Quaternary, influenced by gradual changes in insolation and internal interactions among the atmosphere, oceans, land surfaces and Northern Hemisphere ice sheets (An, 2000; Ding et al., 1994; Kissel et al., 2020; Tian et al., 2010; Wang et al., 2001). These changes have affected the climate and land-ocean energy balance of western Pacific marginal basins, whereas the influence and dynamics of the monsoon system remain insufficiently constrained. Investi-

gations of palaeoclimate variability have significant value in providing valuable insights into monsoonal dynamics across tectonic, orbital and millennial time scales.

Given the importance of the climate signature during the last Glacial Maximum (LGM, spanning approximately 26.5–19 ka) to climate model validation and testing, new reconstructions of precipitation and vegetation response during the LGM are necessary to resolve inconsistencies and improve model reliability. Marine sediments potentially record the interplay of the East Asian Monsoon, surface and deep oceanic circulation and sea level compared with other terrestrial records (Tian et al., 2004; Wang et al., 1999). The SCS is divided into a northern deep basin with isolated, oxygen-poor waters and a southern extensive shelf province, a dichotomy fundamentally controlled by a ∼2400 m deep sill that restricts deep-water exchange with the open Pacific (Chen and Huang, 1996). Due to its well-preserved sedimentary strata, abundant sediment supply, and relatively high sedimentation rates, the northern SCS is recognized as a key area with strong potential for high-resolution palaeoenvironmental reconstructions. Such records can substantially enhance our ability to resolve global and regional climate variability during the Quaternary (Wang et al., 2014). A range of different proxies is preserved in marine sedimentary archives. Pollen evidence, for example, can provide a valuable signal of vegetation evolution on the adjacent continental land mass (Cheng et al., 2023; Luo et al., 2016; Sun et al., 2000a), while microcharcoal particles are widely used in palaeofire reconstruction to infer fire frequency, intensity and vegetation changes, and terrestrial ecosystem response (Conedera et al., 2009). Foraminifera are sensitive to environmental changes, and are widely applied as a palaeo-proxy of marine conditions (Haynes, 1981), although the shells of planktonic foraminifera are susceptible to dissolution which may have limitations. Organic walled dinoflagellate cysts (dinocysts), the resting cysts formed during the sexual reproduction process of these taxa, are characterized by resistant organic matter and are also generally well preserved in marine sediments (Dale, 1996; Zonneveld et al., 2013). The well-known correlation of modern dinocyst distribution with distinct physical marine water properties such as sea surface temperature (SST), salinity, nutrients and productivity indicates the value of dinocysts as a proxy in palaeoceanographic reconstruction, although current research on dinocysts in the SCS remains largely confined to their modern distribution in marine surface sediments (Li et al., 2018a, 2020, 2023). Fossil dinocyst records in the SCS are scarce (Li et al., 2021, 2017).

While previous studies have documented glacial-interglacial changes in vegetation and oceanography in the northern SCS, the relative importance of different forcing mechanisms-particularly the high- and low-latitude forcing across these transitions remain uncertain. To address this, we adopt a multi-proxy approach in this study, combining palynological indicators (pollen, spores, microcharcoal, and dinocysts), organic geochemical proxies (TOC and TN), and inorganic geochemical markers (element ratios, $\delta^{13}C$ and $\delta^{18}O$, and Mg / Ca-based SST of planktonic foraminifera) to reconstruct vegetation, fire regimes, sediment sources, ocean productivity, and sea surface temperature. A marine sediment core (SCS-GC-1; Fig. 1a) recovered from the northern SCS was analyzed to reconstruct millennial-scale climate and ocean dynamics over the last 33 ka. The specific aims of this study are: (1) to reconstruct the palaeovegetation and palaeoclimate; (2) to document the evolution of palaeoceanographic conditions; and (3) to clarify how land-ocean interactions and dominant climate forcings shift across glacial-interglacial transitions.

2 Environmental setting

2.1 Atmospheric circulation and climate

The northern SCS experiences a subtropical to tropical climate with high temperatures (15–28 °C annually): the mean air temperatures range from 15–25 °C during the coldest month (January), and ∼28 °C during the warmest month (July). Rainfall is copious with an annual mean of 1000–2000 mm (Li et al., 2017). The climate is primarily governed by the seasonal East Asian Monsoon system: northeasterly winds prevail during winter (December–February) and southwesterlies dominate in summer (June–August) (Chao et al., 1995; Wang et al., 2017). In winter, decreasing temperatures over the Asian continent lead to the development and intensification of a cold high-pressure system over Inner Mongolia, while the Aleutian Low strengthens over the North Pacific. The resulting continent-ocean pressure gradient drives the East Asian Winter Monsoon (EAWM), transporting cold, dry northeasterly air masses southwards across China into the SCS. In summer, this pattern reverses: the continental system is replaced by the Indian Low, and stronger high-pressure systems develop over the North Pacific and the Australian region, generating the East Asian Summer Monsoon (EASM), which adverts warm, moist-laden air from the ocean onto the Chinese mainland (Liu et al., 2016a).

2.2 Oceanic circulation

Surface currents in the SCS are controlled by seasonal variations in the dominant wind directions related to the EASM and EAWM (Hu et al., 2000), monsoon-topography interactions, and additional influences from wind-stressed eddies. During winter, the EAWM drives a strong southward western boundary current along the Vietnamese and southern Chinese coasts, associated with a basin-scale cyclonic circulation. In contrast, summer circulation is weaker and more complex, with coastal currents generally reversing to flow northward under EASM influence.

The EASM drives distinct northern and southern circulation patterns in the SCS, which form two anticyclonic eddies separated near 12° N by a strong upwelling off Vietnam

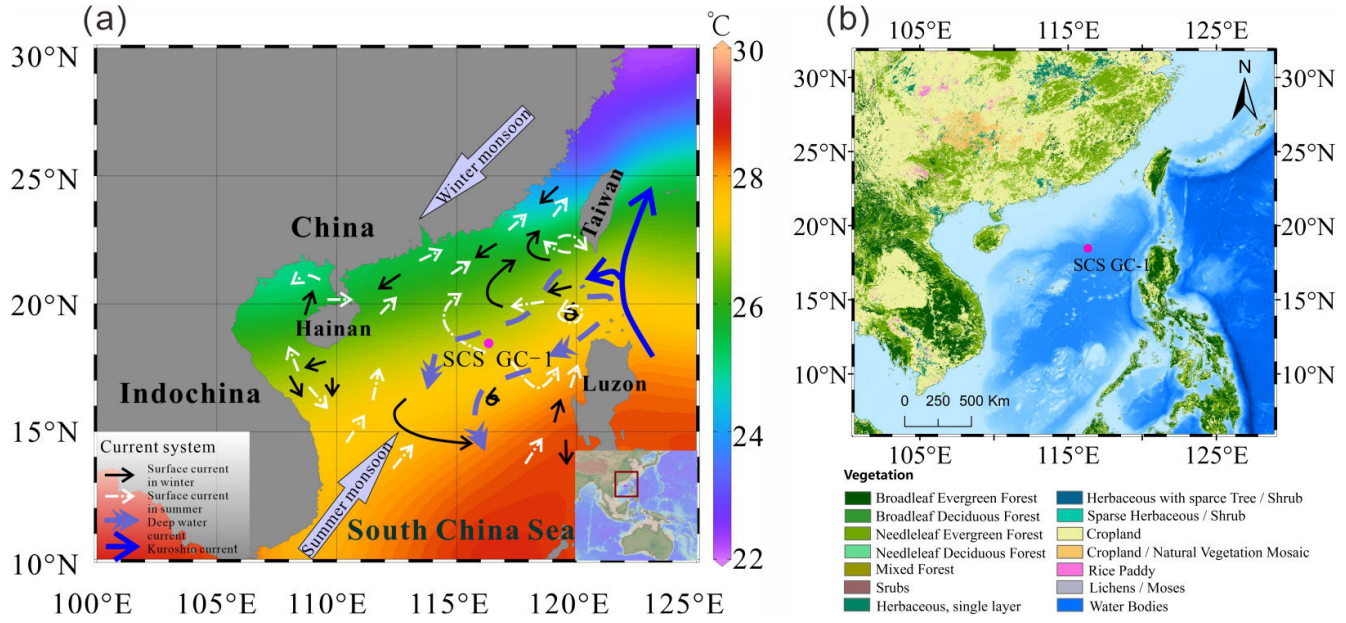

Figure 1. **(a)** Map of the East Asian monsoon system and ocean circulations with annual modern mean annual sea surface temperature (Data from Reagan et al., 2023) and the location of core SCS GC-1 (red) retrieved from the northern SCS. **(b)** Map of the distribution of vegetation types in the main areas around the SCS retrieved from Stibig et al. (2007) and https://forobs.jrc.ec.europa.eu/glc2000 (last access: 22 May 2026). The black solid line indicates the position of the winter surface current, the white dashed line is the position of the summer surface current, the purple dashed line is the deep current, and the blue solid line is the Kuroshio Current.

(Fang et al., 1998). In addition, the region is influenced by the intrusion of warm, saline Kuroshio waters entering through the Luzon strait between Luzon from Taiwan (Huang et al., 2025).

Seasonal variations in marine primary productivity are primarily modulated by the East Asian Monsoon (Liu et al., 2002). During winter, stronger northeasterlies induce eutrophic conditions in the upper euphotic layer, elevating marine primary productivity. In summer, persistent heating of warmer, lower-density surface waters intensifies stratification, leading to oligotrophic conditions and reduced primary productivity (Liu et al., 2002; Zhang et al., 2016).

2.3 Vegetation

Vegetation types on the adjacent continental landmass around the SCS are diverse and reflect regional climate conditions (Luo and Sun, 2013), although they are dominated by tropical and subtropical broadleaved evergreen forests (Fig. 1b) (Stibig et al., 2007). Whereas tropical rain forest vegetation, characterized by taxa such as Dipterocarpaceae, Moraceae, Sapindaceae and Sapotaceae, occurs at low altitudes on tropical islands along the southern coast of the Chinese mainland, e.g., Hainan Island, and southern Taiwan Island. Tropical monsoon forests are distributed widely throughout the Indochina Peninsula and along the coast of southeastern China with the representative species including Verbenaceae, Dipterocarpaceae, as well as pine trees (including *Pinus merkusii*, *Pinus kesiya*, and *Pinus insularis*) which are dominant in the composition of monsoon mountain forest. Subtropical evergreen forests, mainly composed of the families Fagaceae (e.g., *Cyclobalanopsis* and *Quercus*), Lauraceae, and Theaceae, Hamamelidaceae and Magnoliaceae are prominent between 24 and 25° N on southeast-facing hills and on high plateaus (Wang, 1961; Whitmore, 1985). Generally, the abundance of both tropical and subtropical taxa increase gradually towards the south in eastern China, indicating the significance of the north-south temperature gradient (Dai and Weng, 2015; Dai et al., 2015).

The SCS receives enormous amounts of terrigenous sediments (ca. $700 \times 10^6\,\mathrm{t\,yr^{-1}}$) every year, delivered mainly during the rainy season in summer via three major river systems: the Red River, the Pearl River, and the Mekong River (Liu et al., 2010; Milliman and Syvitski, 1992). Among these, the Pearl River, located northeast of the core site, represents a particularly important pathway for transporting terrestrial palynomorphs (including pollen, spores and charcoal) from the adjacent continents to the deep basin. Beyond the river deltas, part of the terrigenous sediments is deposited on the shelves (Zhong et al., 2017), while the rest reaches the open sea where the sediment is transported by the oceanic currents and deposited on the continental slope and in the deep basins (Liu et al., 2013). Consequently, vegetation types occurring in southeast and southern China, as well as Taiwan Island, are the main pollen sources of the northern SCS (Dai and Weng, 2011; Sun et al., 1999).

3 Materials and methods

3.1 Materials and chronological analysis

The 305 cm long marine sediment core SCS GC-1 was retrieved from the northern SCS during R/V *Songhang* (Shanghai Ocean University) cruise in October 2022 (18.47° N, 116.34° E; water depth of 3764 m) (Fig. 1).

Eight accelerator mass spectrometry AMS ^{14}C dates at depths of 20, 45, 65, 90, 107, 133, 203 and 275 cm were obtained on mixed planktic foraminiferal (including *Globigerinoides ruber*, *Globigerinoides sacculifer*, *Neogloboquadrina dutertrei*, *Pulleniatina obliquiloculata*, *Orbulina universa*) tests isolated from the core. AMS ^{14}C measurements were carried out on a NEC 0.5 Mev ^{14}C AMS (National Electrostatics Corporation, NEC) at Guangzhou Institute of Geochemistry, Chinese Academy of Sciences (GIGCAS).

3.2 X-ray fluorescence (XRF) analysis

The core was non-destructively scanned using the Avaatech XRF Core Scanner at the State Key Laboratory of Marine Geology, Tongji University. The parameters of the Avaatech XRF core scanner were set for 30 s exposure time, three voltage and current conditions with 10 kV and 0.75 mA for Al-Fe, 30 kV and 0.5 mA for Co-Mo, and 50 kV and 0.2 mA for Tc-U. The scanning area was 5 mm (length) × 10 mm (width), and at a scanning time of 30 s. The relative content of each element including Al to Ba which was obtained, is expressed in cps as counts per second.

3.3 TOC and TN analysis

Approximately 1 g of each freeze-dried sample was treated with diluted 3 mol L^{-1} HCl for 24 h at room temperature to remove inorganic carbonates. After the reaction, the samples were repeatedly rinsed with ultrapure water (> 18 MΩ cm) and centrifuged until the supernatant reached a neutral pH. The remaining residue was oven-dried at 60 °C, ground and then weighed. The decarbonated samples were analyzed for elemental content using a Vario EL cube elemental analyzer (Elementar, Germany) at the State Key Laboratory of Marine Geology, Tongji University, employing the dry combustion method. Replicate analyses were conducted to ensure data reliability, with average standard deviations of ≤ 0.1 wt % for both TOC and TN measurements.

3.4 Planktonic foraminiferal isotopic and Mg / Ca analysis

The samples were freeze-dried, disaggregated by soaking in water for 1–2 d, then were rinsed repeatedly through a 63 µm sieve to remove organic matter and fine impurities. The rinsed wet samples were then dried at 60 °C (approximately 24 h) and passed through a 125 and 250 µm sieve, respectively (Schönfeld et al., 2012). *G. ruber* larger than 250 µm size were selected under a microscope. For each sample, clean and intact *G. ruber* (around 30 specimens) were picked and tested using a Finnigan MAT253 Mass Spectrometer. The δ^{18}O results are reported versus VPDB after calibration with NBS 19. The average test accuracy is ±0.07 ‰.

For the Mg / Ca analysis, surface dwelling foraminiferal species with smooth-surface individuals of *G. ruber* between 250–350 µm (ca. 0.3 mg) were picked to ensure no obvious contamination or damage, and that the atrioventricular structure was intact (Barker et al., 2003). The analysis was performed on a quadrupole inductively coupled plasma mass spectrometry (ICP-MS). Duplicate measurements of two samples yield an average relative deviation of 0.064 mmol mol^{-1}, confirming that analytical uncertainty is minimal and does not materially affect interpretation. Sea surface temperatures were reconstructed following Eq. (1) (Huang et al., 2008):

$$\mathrm{SST} = 0.5 \times (\ln(\mathrm{Mg/Ca}/0.3)/0.09 + \ln(\mathrm{Mg/Ca}/(0.38 - 0.02 \times D))/0.09) \quad (1)$$

Where SST represents mean annual sea surface temperature (°C), Mg / Ca is the *G. ruber* based Mg / Ca ratio (mmol mol^{-1}), D is water depth of the core (km).

3.5 Palynological analysis

In total, 61 samples (mean interval 4 cm) were processed for palynological analysis at Shanghai Ocean University following standard preparation procedures. Samples were treated sequentially with 10 % HCl, 40 % HF, 30 % HCl, sieved with 125 and 7 µm meshes, and mounted for microscopic examination. Routine identification was performed under a light microscope (ZEISS Promostar 3) at 400 × magnification, with 1000 × used for detailed taxonomic identification. Four *Lycopodium* spore tablets with 10315 ± 845 spores were added to each sample prior to processing to enable calculation of pollen concentration. Pollen taxa were identified using the reference of Tang et al. (2020). At least 300 pollen grains (including terrestrial pollen taxa, sedges and aquatic taxa) were counted for most of the samples. The percentages of pollen taxa were calculated based on the pollen sum excluding *Pinus*, and the percentages of spore taxa were calculated based on pollen and spore sum. The 95 % confidence intervals of percentages were calculated following Maher (1972).

Charcoal particles were identified and counted on the same microscope slides prepared for pollen analysis. Only particles which were black, opaque and angular were considered as charcoal. Particles smaller than 10 µm were not counted due to the risk of false identification (Mooney and Tinner, 2011). More than 1500 charcoal particles (with an average of 3500 particles) were counted for each sample. Two size classes were defined, based on the length of the long axis of each fragment: 10–100 µm is assumed to relate to the re-

gional fire signal and > 100 µm to local fire signals (Conedera et al., 2009).

Organic-walled dinoflagellate cysts (dinocysts) were identified based on Zonneveld et al. (2013), DINOFLAJ3 (Williams et al., 2017), and the online modern dinocyst determination key, viz Zonneveld and Pospelova (2015) and references therein. The percentage of each taxon was calculated based on the total number of dinocysts. The 95 % confidence intervals of percentages were calculated following Maher (1972). All identified dinocyst taxa and their motility affinities are listed in Table S1 in the Supplement. In addition to the above content, foraminiferal organic linings, and other non-pollen palynomorphs such as fungal spores were counted. All counts of pollen, microcharcoal and dinocysts as well as other data discussed in this study have been submitted in the Pangaea database (https://pangaea.de, last access: 22 May 2026) (Felden et al., 2023).

3.6 Statistical analysis

The pollen and dinocyst data were analyzed statistically using the CANOCO software (Canonical Community Ordination: version 5) (ter Braak and Smilauer, 2012). The percentage data used for statistical analysis was not transformed. A Detrended Correspondence Analysis (DCA) was first conducted to test the distribution of the dataset (unimodal or linear). The longest gradient of DCA analysis was found to be 1.1 for pollen data and 1.5 for dinocyst data with standard deviations both less than 3, suggesting that the linear model is more suitable. Accordingly, separate Principal Component Analysis (PCA) were performed to determine the relationship between relative abundances of pollen and dinocyst taxa. Assemblage zones were determined using the constrained cluster analysis (CONISS) in the TILIA (3.0.1) software (Grimm, 2015), which were performed separately, for the pollen (based on a sum excluding *Pinus*) and dinocyst taxa. The top two samples were excluded from the dinocyst CONISS analysis due to insufficient dinocyst counts.

4 Results

4.1 Age-depth model

The eight ^{14}C AMS measurements exhibit a systematic increase in radiocarbon age with sediment depth (Table 1). The age-depth model was constructed using the eight AMS ^{14}C measurements in a Bayesian framework implemented in Bacon (Blaauw and Christen, 2011). A prior accumulation rate of 100 yr cm^{-1} (shape = 1.5, normal distribution) was applied, with the core divided into 52 depth sections of 5 cm. The default memory parameter was retained. Posterior weighted mean calibrated ages were used to derive linear sedimentation rates. The resulting model indicates a basal age of ∼ 33 ka for core SCS GC-1, with sedimentation rates ranging between 0.005 and 0.013 cm yr^{-1} (Figs. 2 and 3a).

4.2 XRF record

The relative contents of these six elements are found for Fe (5×10^3–750×10^3 cps, mean = 540×10^3 cps), Ca (0.7×10^3–650×10^3 cps, mean = 190×10^3 cps), K (1.5×10^3–166×10^3 cps, mean = 91×10^3 cps), Si (1×10^3–144×10^3 cps, mean = 71×10^3 cps) followed by Ti (2×10^3–68×10^3 cps, mean = 41×10^3 cps) and Al (0.5×10^3–14×10^3 cps, mean = 6×10^3 cps) (Fig. S1). Similar patterns among terrigenous elements Fe, K, Ti, Al and Si were observed together with a clearly opposite pattern of marine origin element Ca. The Ti / Al and K / Al show similar patterns with significant correlation ($r = 0.94$, $p < 0.001$) throughout the record (Fig. 3b and c), with low values prior to 16 ka and then increase quickly to much higher values after 16 ka with gradually decreasing trend to the end of the record.

4.3 TOC, TN and TOC / TON record

TOC content and the TOC / TN ratio exhibit significant fluctuations throughout the record (Fig. 3d, e and f). The period prior to 14.7 ka is characterized by high TOC content with low values around 31.2, 22.2, 19.8, 17.9 ka. After 14.7 ka, TOC decreased until 10.4 ka when it increased again to a high level around 6.9 ka followed by a decline trend until the top of the record. Similarly, TOC / TN ratio also exhibits high values prior to 14.7 ka, which then decreased to minimum between 8.8–5.9 ka interrupted by a brief increase around 7.9 ka.

4.4 Planktonic foraminiferal isotopic and Mg / Ca-SST record

The δ^{18}O values of planktonic foraminifera *G. ruber* shells range from −3.2 ‰ to 0.3 ‰ (mean = −1.1 ‰) with higher values prior to 18.7 ka, then started decreasing to much lower values with a short decline around 17.5–14.7 ka (Fig. 3g). The δ^{13}C values range from 0.7 ‰ to 2.5 ‰ (mean = 1.7 ‰) with relatively low values prior to 16 ka (Fig. 3h), there after increasing but with substantial variation.

Mean Mg / Ca-derived SSTs range from 22.1 to 29.7 °C (mean = 24.8 °C) across the core (Fig. 3i). Relatively low values (23.2–25.2 °C, mean = 24.2 °C) occur prior to 21.9 ka, followed by a further decline to the lowest values (22.1–24.6 °C, mean = 23.1 °C) between 21.9–17.5 ka. After 17.5 ka, SSTs increase progressively toward the highest values observed in the record (23.5–29.7 °C, mean = 26.8 °C) with a short decline around 16.6–14.7 ka.

4.5 Palynological record

The complete diagrams of pollen, dinocyst percentages and concentrations, and charcoal results are shown in Figs. S2–S6. Pollen concentration is variable, with particularly high concentrations (390–4100 grains cm^{-3};

Table 1. AMS ^{14}C measurement for mixed planktonic foraminifera from the core SCS GC-1.

Lab #	Depth (cm)	Material	^{14}C age (yr BP)	Calibrated age median (cal. yr BP)	cal. ^{14}C age (cal. yr BP, $\pm 2\sigma$)
GZ10650	20	mixed species	3420 ± 25	3036	1810–4285
GZ10651	45	mixed species	8005 ± 35	8289	7260–9443
GZ10652	65	mixed species	$10\,055 \pm 50$	10 868	9533–12 260
GZ10653	90	mixed species	$13\,090 \pm 70$	14 708	13 392–16 057
GZ10654	107	mixed species	$15\,950 \pm 70$	18 342	17 138–19 485
GZ10655	133	mixed species	$16\,000 \pm 90$	18 399	17 185–19 555
GZ10656	203	mixed species	$20\,540 \pm 170$	23 656	22 496–24 875
GZ10657	275	mixed species	$26\,700 \pm 350$	29 977	28 806–31 063

x yr BP denote before present (1950 AD); all age data were calibrated using the software Calib.Rev.8.10 (Stuiver and Reimer, 1993) and Marine 20 (Hughen et al., 2004). The standard marine reservoir age with a local modification ($\Delta R = 71 \pm 499$ years) in the northern SCS was applied (Wan and Jian, 2014).

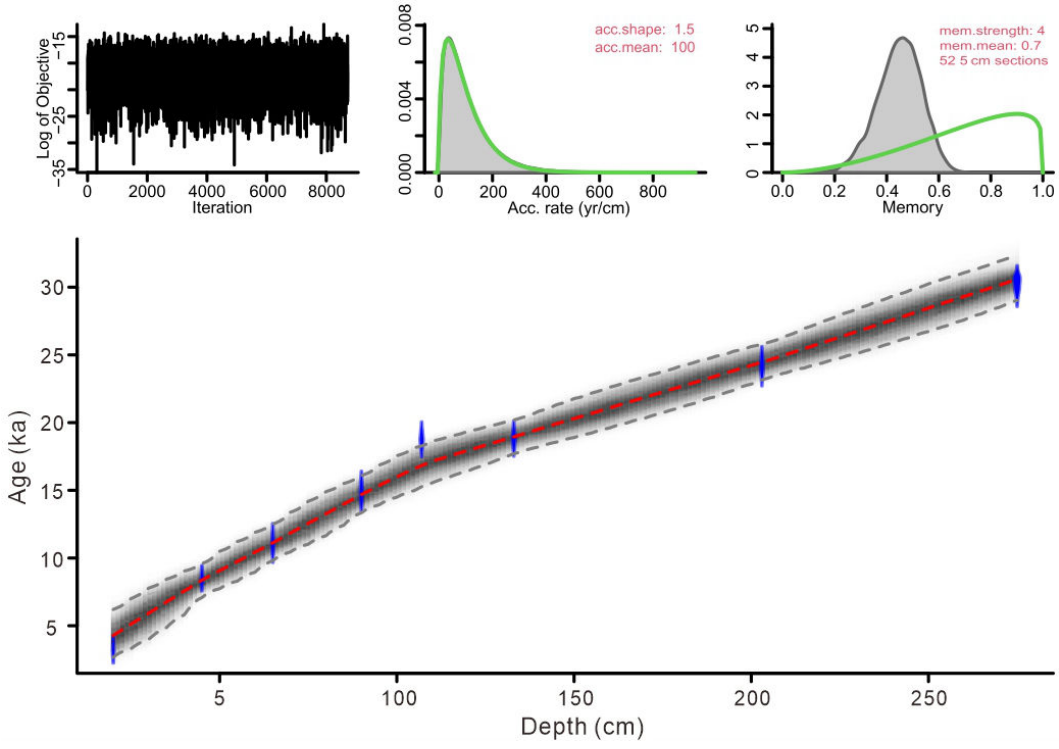

Figure 2. Bayesian age-depth model based on eight AMS ^{14}C dates from core SCS GC-1: the blue areas represent the 95 % probability distributions of the calibrated ages; the thin red line shows the weighted mean ages, and the blackish-gray area shows the 95 % age-depth relations as modeled by the R software package Bacon 2.2 (Blaauw and Christen, 2011).

mean = 1200 grains cm^{-3}) prior to 16.1 ka, and highest concentrations around 25.3–25.0 ka (3300–4100 grains cm^{-3}; mean = 3700 grains cm^{-3}) (Fig. 4). Similarly, charcoal exhibits the highest concentrations (36–155 × 103 particles cm^{-3}; mean = 83×10^3 particles cm^{-3}) around 25.3–23.7 ka, decreasing after 15.6 ka, reaching minimum values at the top of the core (9–31×10^3 particles cm^{-3}; mean = 21×10^3 particles cm^{-3}) (Figs. 4 and S6). Dinocyst concentrations are relatively low, ranging from 7–1600 cysts cm^{-3} (average of 450 cysts cm^{-3}) with high values of 110–1600 cysts cm^{-3} (average of 650 cysts cm^{-3}) between 25.6–11.7 ka (Figs. 4 and S5). After 11.7 ka, dinocyst concentrations decrease, reaching a minimum at the end of the record.

According to the PCA results (Fig. 5a), pollen and spore taxa are well-separated based on their associated biomes. Specifically, *Pinus* and fern spore (notably *Hicriopteris*, *Pteris*, Polypodiaceae and Cyathaceae) form a distinct cluster on the positive end of axis 1, while characteristic terrestrial herbs (particularly *Artemisia*, Poaceae and Cyper-

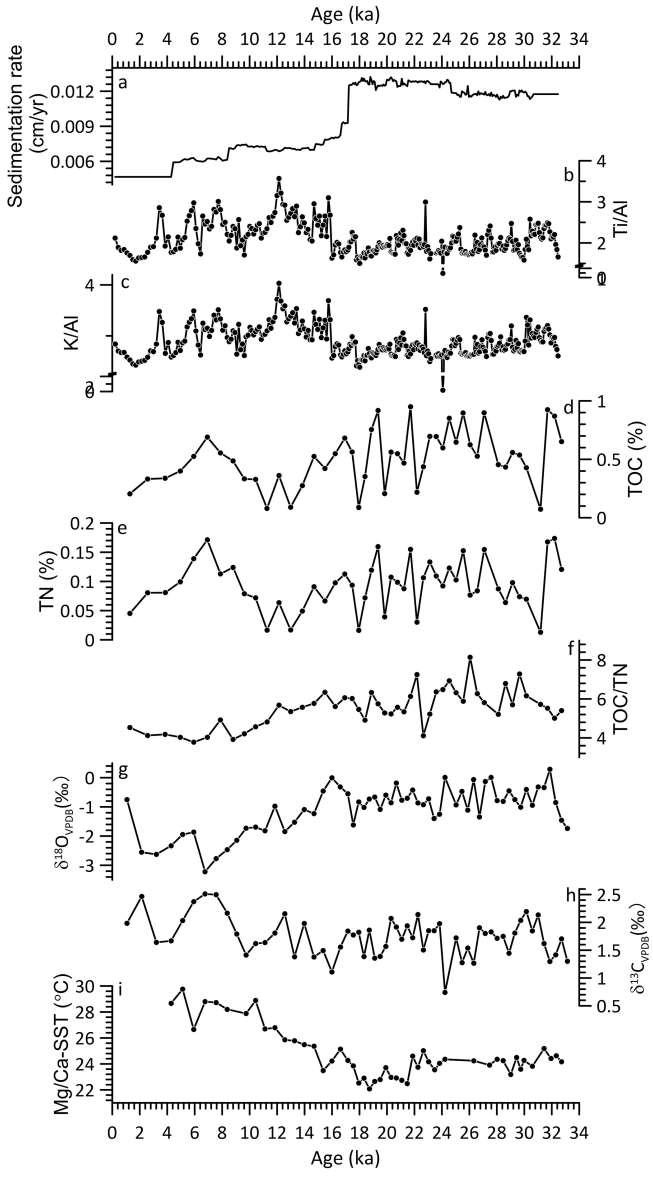

Figure 3. Core SCS GC-1 sedimentation rate **(a)**, major element ratio **(b–c)**, contents of total organic carbon (TOC, **d**) and nitrogen (TN, **e**), TOC / TN ratio **(f)**, stable oxygen isotope $\delta^{18}O_{VPDB}$ **(g)** and stable carbon isotope $\delta^{13}C_{VPDB}$ **(h)** isotopes from planktic foraminifera, and Mg / Ca-SST **(i)**.

aceae) are separated along the negative end of axis 1 and relatively positive side of axis 2. Three groups of dinocyst taxa can be distinguished based on the PCA results, showing clearly different trends across the record (Fig. 5b). Group 1: *Operculodinium. centrocarpum*, *Impagidinium* spp., *Impagidinium aculeatum*, *Impagidinium patulum*, *Impagidinium paradoxum*, *Impagidinium strialatum*, *Impagidinium* type1; *Bitectatodinium spongium*; Group 2: *Brigantedinium* spp.; Group 3: *Echinidinium* spp., *Echinidinium aculeatum*, *Echinidinium transparantum*, *Selenopemphix nephroides*, *Stellasinium stellatum*; *Selenopemphix quanta*, *Dubridinium* spp., *Operculodinium israelianum*; *Operculodinium* spp., *Lingulodinium machaerophorum*, *Tuberculodinium vancampoae*, *Spiniferites mirabilis*, *Spiniferites* spp.; *Spiniferites bentori*.

Separate CONISS analysis were performed for pollen and dinocyst data, with results shown in Figs. S2 and S4. Considering that the zonations based on pollen and dinocyst data show very similar results, five main zones can be recognized in the record for the purpose of synthesizing the multi-proxy climatic signal (Fig. 4).

4.5.1 Zone 1 (301–237 cm, 32.8–27.3 ka)

This zone is characterized by relatively high percentages of *Pinus* and evergreen *Quercus*, while pollen taxa of terrestrial herbs such as *Artemisia*, Poaceae and Cyperaceae as well as fern spores including *Hicriopteris*, Polypodiaceae, Cyathaceae are relatively low (Figs. 4 and S2). High fungal spore concentrations here coincide with low charcoal concentrations. The percentages of heterotrophic taxa *Brigantedinium* spp. (Group 1) increase gradually to the end of this zone, whereas the percentages of autotrophic taxa (Group 2) particularly *Impagidinium* species reach their maximum levels in the record but decline towards the end of this phase (Figs. 4 and S4). Concentrations of foraminiferal organic linings reach minimum in this zone.

4.5.2 Zone 2 (237–109 cm, 27.3–17.0 ka)

The percentage of *Pinus* pollen decreases to its lowest values of the entire record. Meanwhile, terrestrial herb taxa, particularly *Artemisia*, increase to their highest levels along with fungal spores. Some fern spore types, including Polypodiaceae, Hymenophyllaceae, Cyatheaceae and *Pteris*, also exhibit relatively high values compared to Zone 1 (Figs. 4 and S2). Concentrations of pollen, fern spores and charcoal all reach maximum values, peaking around 25.3–24.3 ka when dinocyst concentrations also exhibit a maximum, along with *Brigantedinium* spp. On the other hand, Group 1 dinocyst taxa are at minimum values in this zone. Concentrations of foraminiferal organic linings remain at low value in this zone.

4.5.3 Zone 3 (109–89 cm, 17.0–14.5 ka)

In comparison to Zone 2, Zone 3 is marked by a slight increase of *Pinus* and decrease in herb pollen. Both pollen and charcoal concentration exhibit slight decreasing trend. Concentrations of fungal spores exhibit a declining trend and return to the levels observed in Zone 1. Dinocyst concentrations quickly decrease to relatively low values. While *Brigantedinium* spp. remain high values, other taxa such as *Echinidinium* spp., *Echinidinium aculeatum* and *Spiniferites* species exhibit minimum values.

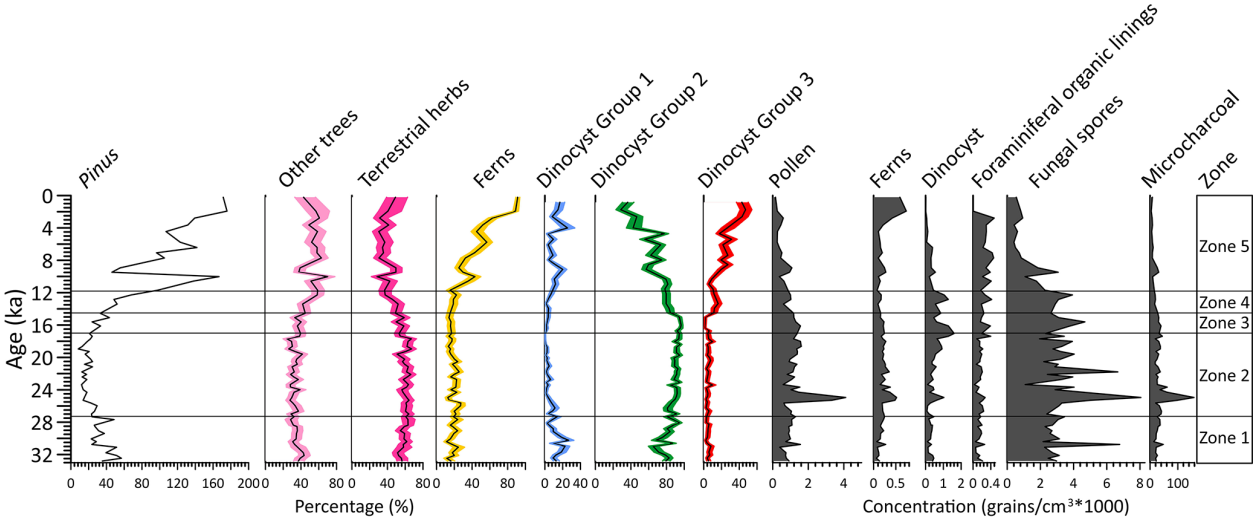

Figure 4. Percentages (%) of dominated pollen taxa, including pollen of *Pinus*, other trees, terrestrial herbs, fern spores, and three dinocyst groups based on principal component analysis (PCA) analysis, concentrations (grains $cm^{-3} \times 1000$) of pollen, fern spores, dinocyst, foraminiferal organic linings, fungal spores and microcharcoal concentration (particles $cm^{-3} \times 1000$).

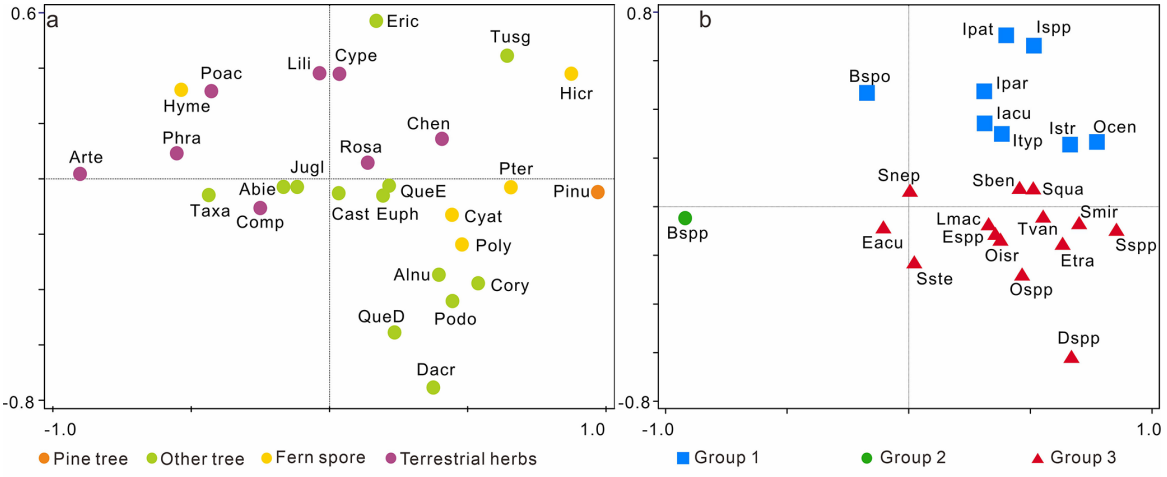

Statistic	Axis 1	Axis 2	Axis 3	Axis 4
Eigenvalues	0.64	0.070	0.04	0.03
Explained variation (cumulative)	64.45	71.23	75.26	78.35

Statistic	Axis 1	Axis 2	Axis 3	Axis 4
Eigenvalues	0.36	0.21	0.08	0.05
Explained variation (cumulative)	36.45	57.78	65.51	70.15

Figure 5. Results of the principal component analysis (PCA) illustrating the ordination of pollen **(a)** and dinocyst taxa **(b)** from core SCS GC-1 with colored symbols referring to the groups. For pollen, pine tree (orange): Pinu (*Pinus*); other tree (light green): QueE (*Quercus* evergreen), QueD (*Quercus* decedious), Alnu (*Alnus*), Podo (Podocarpaceae), Dacr (*Dacrycapus*), Taxa (Taxaceae), Abie (*Abies*), Tusg (*Tusga*), Eric (Ericaceae), Jugl (*Juglans*), Cory (*Corylus*), Cast (*Castanea*), Euph (Euphorbiacae); fern spores (yellow): Hicr (*Hicriopteris*), Pter (*Pteris*), Cyat (Cyatheaceae), Poly (Polypodiaceae), Hyme (Hymenophyllaceae); terrestrial herbs (purple): Arte (*Artemisia*), Poac (Poaceae), Cype (Cyperaceae), Comp (Compositae), Phra (*Phragmites*), Chen (Chenopodiaceae), Rosa (Rosaceae), Lili (Liliaceae). For dinocyst groups, Group 1 (blue): Ocen (*O. centrocarpum*), Ispp (*Impagidinium* spp.), Iacu (*Impagidinium aculeatum*), Ipat (*Impagidinium patulum*), Ipar (*Impagidinium paradoxum*), Istr (*Impagidinium strialatum*), Ityp (*Impagidinium* type 1), Bspo (*Bitectatodinium spongium*); Group 2: Bspp (*Brigantedinium* spp.); Group 3: Espp (*Echinidinium* spp.), Eacu (*Echinidinium aculeatum*), Etra (*Echinidinium transparantum*), Snep (*Selenopemphix nephroides*), Sste (*Stellasinium stellatum*), Squa (*Selenopemphix quanta*), Dspp (*Dubridinium* spp.), Oisr (*Operculodinium israelianum*), Ospp (*Operculodinium* spp.), Lmac (*Lingulodinium machaerophorum*), Tvan (*Tuberculodinium vancampoae*), Sben (*Spiniferites bentori*), Smir (*Spiniferites mirabilis*), Sspp (*Spiniferites* spp.).

4.5.4 Zone 4 (89–69 cm, 14.5–11.7 ka)

Zone 4 is characterized by the rapid increase in *Pinus* pollen, accompanied by a sharp decline in terrestrial herbs, especially *Artemisia*. Concentrations of pollen, fern spores and charcoal also exhibit a declining trend to reach near the lowest levels, whereas dinocyst concentrations remain relatively prominent. However, the percentage of *Brigantedinium* spp. exhibits a decline in this zone, accompanied by a marked increase of Group 3 taxa, including *Dubridinium* spp. and *Echinidinium* spp. Meanwhile, dinocysts in Group 2 achieve relatively high values. Concentrations of foraminiferal organic linings increase gradually from the beginning of this zone.

4.5.5 Zone 5 (69–0 cm, 11.7 ka–present)

The percentages of *Pinus* pollen reach their highest values of the entire record interrupted around 9.5–9.0 ka by a very marked decline to values close to those of Zone 1. The abrupt reduction in *Pinus* pollen is also observed in the overall pollen, fungal spore, charcoal concentration, and in terrestrial herb pollen especially. Additionally, this zone is characterized by the increase in fern spores, particularly *Hicriopteris* which exhibits a short, sharp increase around 2.8 ka (Figs. 4 and S2). The percentage of *Brigantedinium* spp. decreases to the lowest values of the entire record, whereas the percentage of Group 3 dinocyst taxa, along with the concentration of foraminiferal organic linings all reach their highest values.

5 Discussion

5.1 Environmental significance of key proxies

5.1.1 K / Al and Ti / Al

In comparison to single elements, elemental ratios which are insensitive to dilution effects, are more useful as environmental indicators (Govin et al., 2012). Ti is highly enriched in mafic and volcanic rocks, while Al is a major component of most common clay mineral found in all types of weathered continental crust. The SCS is surrounded by diverse geological terrains with distinct Ti / Al ratios originating from different sources such as the Luzon Volcanic Arc (Philippines), Taiwan and other basaltic sources with high Ti / Al, while with low Ti / Al originating from the major continental river systems that drain ancient, weathered landmasses. Thus, Ti / Al can provide a robust picture of terrestrial input and its origin in the complex environment of the SCS. High Ti / Al indicates increased relative input of sediment from a volcanic or mafic source/less chemical, and low Ti / Al indicates increased relative input of sediment from a felsic continental source (e.g., Pearl River, Mekong River) (Hu et al., 2013; Wan et al., 2007). K / Al and Ti / Al records of ODP Site 1143 from the SCS generally show low values during glacial periods and high values during interglacial periods, clearly indicating that increase in K / Al and Ti / Al is probably related to wetter conditions and thus the intensified chemical weathering (Clift et al., 2008; Tian et al., 2011; Wei et al., 2004).

5.1.2 Source area and transport of pollen and spores

In the northern SCS sediments, the modern distribution of tree pollen, particularly *Pinus*, shows disproportionately high representation relative to other pollen types. This suggests substantial contributions from south and southeast China, transported primarily by the northeasterly winter monsoon and associated wind-driven currents. While elevated *Pinus* percentages can signal either a strengthened winter monsoon or a cool, humid climate (Luo et al., 2018; Sun et al., 2003), PCA results (Fig. 5a) indicate that this ambiguity can be resolved by incorporating fern spore data. Unlike wind-dispersed *Pinus* pollen, the larger, heavier spores of ferns are primarily transported by river runoff. Their high abundance in sediments therefore signals a proximal source from humid montane forests (e.g., in Taiwan and southern China), reflecting a humid climate controlled by the EASM (Kaars et al., 2000; Sun et al., 2000b; Wang et al., 2009). Consequently, a simultaneous peak in both *Pinus* pollen and fern spores is incompatible with a scenario of solely strengthened, dry winter winds. Instead, this combined signal robustly indicates a cool and humid climatic regime. In this regime, a vigorous EASM delivered high rainfall, which promoted fern-rich vegetation and riverine spore transport, while the EAWM remained active enough to distribute *Pinus* pollen without dominating the climatic regime. Therefore, we propose a possible interpretation for the low *Pinus* during the glacial period and high *Pinus* during the interglacial period: during the glacial period especially during the LGM, a strong but dry EAWM could efficiently transported *Pinus* pollen from distant montane source areas. However, local arid conditions on the exposed continental shelf limited the growth of conifers near the core site leading to moderate percentages in the record; during the interglacial period especially during the Holocene, despite the increased distance due to sea-level rise, enhanced EASM-driven humidity favoured the expansion of Pine forests in source regions. Concurrently, altered atmospheric and oceanic circulation patterns likely facilitated the long-distance transport of pollen to the deep basin.

Artemisia, Poaceae and Cyperaceae pollen are the main components of terrestrial herbs observed in the core. *Artemisia* spp. is currently widely distributed in temperate grassland and steppe which is associated with cool, semi-arid conditions (Bandara et al., 2023; Sun et al., 2003). Although Poaceae and Cyperaceae pollen indicate a range of different habitats, high percentages of Poaceae pollen in the sediment are suggestive of grassland vegetation, and a high representation of Cyperaceae pollen can point to wetland environments, though in association with *Artemisia* and Poaceae, it

may also form part of dry grassland communities (Sun et al., 2003; Wang et al., 2009).

Previous studies have found clear temporal variations in pollen assemblages in the SCS characterized by marked higher pollen concentrations in glacial sediments than in interglacial sediments (Jiwarungrueangkul and Liu, 2021; Sun et al., 2000a; Sun and Luo, 2001; Sun et al., 2003; Zheng and Lei, 1999). On one hand, the large amount of pollen in glacial sediments at the site might be transported by a strengthened northeast winter monsoon from the Asian mainland and Taiwan Island. In contrast, during the last glacial low stand, sea level was 120–150 m lower than today, exposing much of the northern SCS continental shelf and increasing land area by roughly $24 \times 104\,km^2$ (Chen et al., 2020; Sun et al., 2000a; Wang et al., 2009). The northern SCS would likely receive substantial pollen and spore amounts via wind or water from the exposed continental shelf which was covered by grassland under the prevailing dry and temperate climate of the time (Luo and Sun, 2005; Sun et al., 2003). This expansion of open, terrestrial herb-dominated vegetation likely occurred on both the exposed shelf and the adjacent continental catchments due to the overall drier glacial climate. Typically, during glacial periods, herbaceous vegetation is predominant in the region, whereas during interglacial periods tree and ferns dominate the terrestrial land mass adjacent to the SCS (Sun et al., 2000a; Sun and Luo, 2001). Such glacial-interglacial transitions are driven by changes in climate, or ocean currents, or both. During MIS 2 (21–11.5 ka), *Artemisia* increased again and occupied most of the extensive emerged continental shelf (Sun et al., 2003). Accordingly, the ratio of trees / herbs pollen is a valuable indicator of glacial-interglacial cycles along with their associated vegetation and climate conditions.

5.1.3 Dinocysts

Although modern dinocyst distributions are strongly correlated with sea surface conditions such as sea surface temperature, sea surface salinity, nutrient levels and productivity (Dale, 1996; Marret and Zonneveld, 2003; Zonneveld et al., 2024), dinocyst deposition and preservation in marine sediments are affected by various non-ecological, taphonomic factors which may alter the primary dinocyst accumulation in the sediment (Holzwarth et al., 2007). It is therefore crucial to account for these factors before relating the fossil dinocyst record to palaeoenvironmental conditions. Upwelling off west Luzon is driven by the EAWM and intensifies during stronger EAWM phases. This process brings nutrient-rich subsurface waters to the surface, promoting enhanced dinoflagellate production (Yuan et al., 2004). The Kuroshio Current, which transports warm and high-salinity water into the northern SCS leading to a significant increase in sea surface temperature, is also a significant factor influencing dinoflagellate growth. Additionally, heterotrophic taxa, such as degradation-sensitive species from the *Protoperidinium* genus, are more susceptible to aerobic degradation compared to autotrophic taxa (Holzwarth et al., 2007). This may be influenced by the water oxygen content which may therefore alter dinocyst assemblages before and after sedimentation (Zonneveld et al., 2008). However, the persistent dominance of heterotrophic dinocysts in the record (up to 99 % with mean values of 85 %) suggests that selective dissolution of protoperidiniacean species relative to other taxa in the sediments is negligible (Zhao et al., 2017).

Impagidinium cysts as well as *O. centrocarpum* typically indicate open ocean, fully marine settings characterized by low primary productivity, low nutrient levels, and well-oxygenated bottom waters (Zonneveld et al., 2013; Zonneveld and Pospelova, 2015). Modern surface dinocyst distribution in SCS shows that most of *Impagidinium* species, *Nematosphaeropsis labyrinthus* and *Polysphaeridium zoharyi* are positively correlated with water depth. Their highest abundances were observed in the northern slope-deep basin which is influenced by the Kuroshio Current, indicating an open-ocean environment (Li et al., 2020). In the northern Philippine Sea, the predominance of *Impagidinium* taxa from the bottom sediments is also indicative of pelagic and tropical regions (Matsuoka, 1981). During winter, the Kuroshio Current transports high-salinity, low-nutrient waters from the Philippine Sea through the Luzon Strait, which then flows along the continental shelf break, reaching the study area in the northern SCS. This provides further evidence that the increased abundance of Group 1 taxa may reflect typical nutrient-poor open ocean environments and enhanced influence of the Kuroshio Current. Dinocysts preserved in SCS GC-1 are dominated by *Brigantedinium* spp. (28 %–96 %, mean = 80 %), which have also been observed from sediment trap samples in the southwest Taiwan waters of the SCS with high representation ranging from 68 % to 91 % (Li et al., 2018b). High abundances of *Brigantedinium* spp. are characteristic of increased nutrient supply (Dale, 1996), which has been used as an indicator of primary productivity (Li et al., 2020; Zonneveld et al., 2013). In addition, *Brigantedinium* spp. is usually more abundant near the winter upwelling zone in the SCS (Li et al., 2020). Therefore, Group 2 taxa, characterized by the dominance of *Brigantedinium* spp., indicates intensified upwelling conditions with strong terrigenous influence that contrasts with open-ocean oligotrophic conditions indicated by Group 1. The stratigraphic variation of Group 2 cysts (Fig. 6h) displays an inverse relationship with Mg / Ca-SST, supporting the glacial "high-productivity/low-temperature" paradigm. Group 3 taxa, characterized by dinocysts such as *Echinidinium* spp. and *S. quanta* are typically adapted to fully marine, eutrophic, and highly productive regimes, and are likely indicative of water column stratification and upwelling processes in open ocean environments (Zonneveld et al., 2013). The shift from Group 2 to Group 3 dominance during the deglaciation may thus signal a transition from terrestrial nutrient-driven pro-

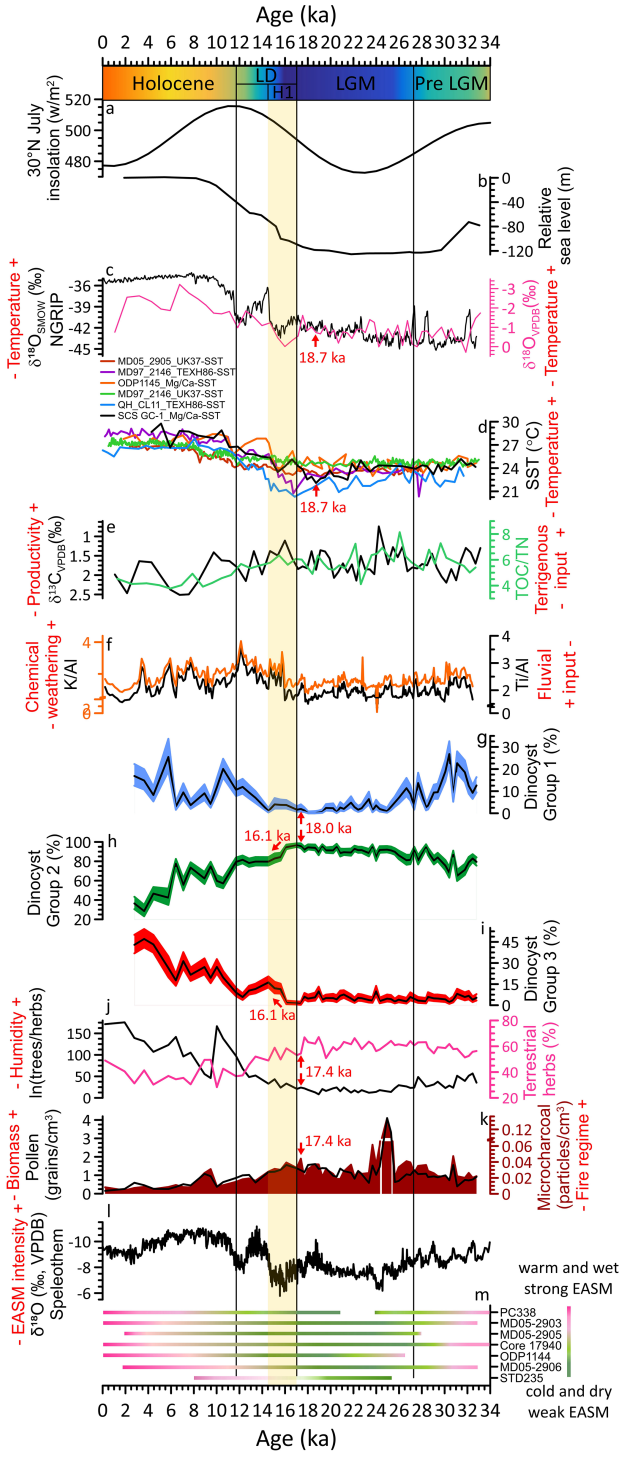

Figure 6. 30° N July insolation (Laskar et al., 2004) **(a)**; relative sea level on the Sunda Shelf, SCS (Hanebuth et al., 2000) **(b)**; NGRIP $\delta^{18}O_{SMOW}$ (North Greenland Ice Core Project members, 2004) (**c**, black) and stable oxygen $\delta^{18}O_{VPDB}$ of planktonic foraminifera from SCS GC-1 (**c**, pink); SST records from MD052905 (Zhou et al., 2012), MD972146 (Lin et al., 2014), ODP1145 (Oppo and Sun, 2005), QHCL11 (Liu et al., 2020) and SCS GC-1 **(d)**; stable carbon $\delta^{13}C_{VPDB}$ of planktonic foraminifera (**e**, black) and TOC / TN ratio (**e**, green); major element ratio Ti / Al (**f**, black) and K / Al (**f**, orange), percentages of three dinocyst groups **(g, h, i)**; ratio of trees / herbs (**j**, black) and percentages of terrestrial herbs (**j**, pink); pollen concentration (**k**, black) and microcharcoal concentration (**k**, dark red shading); compilation of speleothem $\delta^{18}O_{VPDB}$ values from central China **(l)** (Cheng et al., 2016); summary of records indicating climate and potential intensity of EASM **(m)** (Sun et al., 2000a, b; Luo and Sun, 2005; Zhou et al., 2012; Xie et al., 2014; Dai and Weng, 2015; Dai et al., 2015; Yu et al., 2017; Li et al., 2019). Pre LGM: pre Last Glacial Maximum; LGM: Last Glacial Maximum; LD: last deglaciation; H1: Heinrich Stadial 1. Red arrows indicate the onset of the transition in different proxies.

ductivity to a more stratified, marine-dominated productivity regime.

5.2 Shelf exposure, aridity and high marine productivity during the LGM

Over the past 33 ka, five CONISS-derived statistical zones are grouped into four distinct climatic phases (Fig. 6): pre-LGM (Zone 1, 32.8–27.3 ka), LGM (Zone 2, 27.3–17.0 ka), last deglaciation (Zones 3 and 4, 17.0–11.7 ka), and Holocene (Zone 5, 11.7 ka–present) (Figs. 4 and 6). This sequence reveals a pronounced glacial-interglacial transition. The relatively cooler and drier glacial regime during 32.8–27.3 ka was defined as pre-LGM. The climatic condition became more pronounced during 27.3–17.0 ka, which was characterized by markedly higher sedimentation rates (Fig. 3a), cooler SST (by ca. 3.3 °C on average, Fig. 6c and d), higher primary productivity (Fig. 6e and h), reduced humidity (Fig. 6f, j, l and m), a landscape dominated by herbaceous vegetation (Fig. 6j), and strengthened fire activity (Fig. 6k). We refer this interval to the LGM representing the regional expression of glacial conditions in the northern SCS, which is longer than the globally defined LGM (26.5–19.0 ka) (Clark et al., 2012), but consistent with other marine records from the western Pacific marginal seas (Sun et al., 2000a; Wang et al., 2009).

During the LGM, sea levels were approximately 120 m lower than present, leading to extensive exposure of the northern SCS continental shelf (Fig. 6b), which effectively extended the coastal plains and created an expansive, low-relief terrestrial surface (Hanebuth et al., 2000). While previous studies have attributed elevated charcoal and pollen concentrations during the LGM to the reduced distance to sediment sources from this exposed continental shelf (Luo and Sun, 2005; Sun et al., 2000a), our multi-proxy data support this proximal-source effect and further demonstrate that the vegetation colonizing the shelf was fundamentally shaped by the cold and dry glacial climate. Specifically, the high percentages of terrestrial herb pollen, in particular arid-tolerant *Artemisia* together with Poaceae and Cyperaceae, minimum tree pollen (Fig. S2), and trees / herbs ratio (Fig. 6j) all indicate a herbaceous landscape. Moreover, independent climate proxies also confirm the arid conditions: the low K / Al ratio (Fig. 6f) suggesting reduced chemical weathering under drier conditions, aligns with the enriched speleothem $\delta^{18}O$ values indicating a weakened EASM and reduced rainfall over the region (Fig. 6l) (Cheng et al., 2016). This aridity suppressed forest growth and favoured drought-tolerant herbs. Concurrently, the maximal concentrations of microcharcoal (Fig. 6k), especially the large charcoal particles (> 100 µm) indicative of local fires (Fig. S6), coincide with maximal herb pollen. This is ecologically explainable: herbaceous vegetation especially in dry seasonal climate could produce fine, highly flammable fuel that supports frequent and potentially high-intensity fires (Zanzarini et al., 2022). Therefore, the high terrestrial herb pollen percentage reflects a dual control: the exposed shelf provided a vast proximal source area, while the glacial climate determined that this area and possibly the adjacent continental catchments would be occupied by drought-adapted grassland/steppe vegetation.

The substantially shortened distance between the exposed shelf and the core site (Lambeck et al., 2014) would have facilitated more efficient transfer of terrigenous nutrients to proximal deep-sea areas. The low Ti / Al ratios (Fig. 6f) suggest that this enhanced input originated mainly from felsic continental rivers (e.g., the Pearl River). Although weakened EASM would typically suppress fluvial discharge, this effect appears to have been offset by the closer coastline and the likely persistence of eolian dust transport from the arid Chinese mainland. Concurrently, this open landscape, combined with likely enhanced erosion under such variable glacial conditions would have supplied abundant terrestrial nutrients to the adjacent ocean. Enhanced terrigenous nutrient delivery from this expansive, herb-covered continental shelf and arid continental hinterlands also appears to have stimulated elevated marine productivity during the LGM. This is clearly recorded in our marine proxies: TOC / TN ratio with a range between 3.8–8.1 throughout the record indicates a marine phytoplankton-dominated organic matter source (Meyers, 1997), while elevated $\delta^{13}C$ values of planktonic foraminifera (Fig. 6e) during this period suggest enhanced organic carbon export. Critically, the combined fluvial and eolian nutrient fluxes would have created a nutrient-replete surface ocean, directly favouring heterotrophic dinoflagellates such as *Brigantedinium* (Smayda and Trainer, 2010). This can thereby well explain the dinocyst record characterized by pronounced dominance of dinocyst Group 2 (*Brigantedinium* spp. which can constitute up to 97 %, mean = 81 %) indicative of high nutrient availability, alongside the near-absence of oligotrophic, open-ocean Group 1 (Fig. 6g and h), points to a productivity regime sustained by abundant terrestrial nutrient supply rather than open-ocean processes. This pattern is consistent with global compilations showing that organic carbon accumulation rates during glacial maxima were ∼ 50 % higher than interglacial intervals (Cartapanis et al., 2016). Independent evidence from the northern SCS similarly links higher glacial productivity to intensified winter monsoon winds, enhanced water-column mixing, upwelling, and increased land-derived nutrient supply (Xu et al., 2025). Our dinocyst record, characterized by the dominance of a heterotrophic, highly nutrient-dependent taxon, strongly supports the interpretation that terrestrial nutrient supply was a key mechanism together with the complementation of the physical forcing of strengthened winter monsoon-driven mixing.

5.3 Early ocean warming, monsoon intensification and ecosystem response since the last deglaciation

Since the last deglaciation, the northern SCS has experienced a comprehensive environmental transformation characterized by decreasing sedimentation rates, rising SST, declining primary productivity, increased moisture availability, a pronounced expansion of pine forests, and reduced fire activity. Critically, our record reveals that the initial signal of this transformation was an SST increase at ca. 18.7 ka (Fig. 6c and d) (North Greenland Ice Core Project members, 2004; Lin et al., 2014; Liu et al., 2020; Oppo and Sun, 2005; Zhou et al., 2012), which began ∼ 1.3 ka earlier than the major shifts in terrestrial vegetation and other sediment proxies (ca. 17.4 ka, Fig. 6j and k). This early ocean warming provides direct, local evidence for the primacy of ocean-atmosphere forcing in initiating the regional deglacial transition. Additionally, the millennial-scale event of H1 (17.0–14.5 ka) is embedded within the early phase of this warming, recorded as an interval of low SST, high $\delta^{18}O_{VPDB}$ of planktonic foraminifera and high percentages of terrestrial herb pollen. This interval interpreted as the regional expression of H1 in the northern SCS, falls within the broader range of published H1 chronologies (17.5–14.5 ka, Denton et al., 2006; 18–15.6 ka, Sánchez Goñi and Harrison, 2010) and is consistent with other western Pacific records (Xu et al., 2013). This suggests that short-period cold and dry conditions linked to North Atlantic forcing temporarily modulated but did not override the underlying tropical warming trend in the study area (Clark et al., 2012). However, the Bølling–Allerød (B–A, 14.5–12.9 ka) and Younger Dryas (YD, 12.9–11.7 ka) are not clearly identified in our proxies. Instead, our record shows a progressive trend toward warmer, wetter, and more forested conditions from 14.5 ka onward, without distinct reversals or plateaus.

The earlier onset of SST warming corresponds more closely with rising boreal summer insolation (Fig. 6a) (Laskar et al., 2004) than with the rate of sea-level rise (Fig. 6b) (Hanebuth et al., 2000). This implies that tropical ocean warming, likely amplified by ocean-atmosphere feedbacks, acted as the initial trigger for subsequent environmental changes. This effect is especially pronounced in the tropics and is consistent with the concept of tropical ocean-atmosphere forcing (Cheng et al., 2019; Xie et al., 2010). For instance, seminal work has shown that the timing of peak East Asian Monsoon intensity differs between marine and terrestrial records (An et al., 2000). Furthermore, while terrestrial pollen records from East Asian indicate rapid warming around 15 ka, synchronous with Greenland ice core and stalagmite records from southern China, marine SST reconstructions (based on Mg / Ca-SST and long chain alkenone $U^{k'}_{37}$-SST) from the same record indicate that SSTs began to rise as early as 20–19 ka, a trend more consistent with the early warming of the Western Pacific Warm Pool (Xu et al., 2013). This 3–4 kyr lag of terrestrial warming behind western Pacific oceanic warming highlights the differential thermal response and reinforces the interpretation that early ocean warming served as a critical forcing mechanism.

The sequence of multi-proxy changes in our record reveals a clear mechanistic chain initiated by this early SST rise. The first detectable response in our marine proxies is a shift in dinocyst assemblages at ca. 18.0 ka, marked by the incipient increase of oligotrophic Group 1 dinocysts and the onset of decline in the highly nutrient-dependent Group 2 dinocysts. We attribute this to a direct oceanographic response to warming: enhanced upper water column stratification reduced vertical nutrient supply, favoring oligotrophic taxa over heterotrophic ones. Subsequent to this initial marine response, the physical reconfiguration of the coastline due to sea level rise further modulated the environmental trajectory. The inundation of the exposed continental shelf increased the distance from terrestrial sediment sources to the core site (Luo and Sun, 2005; Sun et al., 2000a) and created a sediment trap on the newly formed shallow marine environments, leading to a dramatic reduction in terrigenous material reaching our deep basin site (Liu et al., 2003; Wang and Sun, 1994). This is reflected in markedly lower sedimentation rates and increased Ti / Al ratios (Figs. 3a and 6f), indicating reduced terrestrial input. The combination of sustained ocean warming and reduced nutrient supply further suppressed heterotrophic dinoflagellates such as *Brigantedinium* (Smayda and Trainer, 2010), driving a pronounced decline in Group 2 dinocysts from 16.1 ka and a concurrent increase in Group 3 dinocysts which is indicative of more stratified, marine-dominated conditions (Fig. 6h and i), coincident with a reduction in TOC / TN (Fig. 6e). This shift marks a fundamental transition in the productivity regime: from a terrigenous nutrient-driven regime (Group 2 dominated during the LGM) to a more stratified, marine-dominated regime (Group 3).

Parallel to these oceanic changes, the shrinking continental shelf also constrained the habitat for herbaceous vegetation. Concurrently, the intensification of the EASM, a large-scale atmospheric response like initiated and reinforced by the warming tropical ocean and the evolving land-sea thermal contrast, is recorded by the rapid negative shift in the speleothem $\delta^{18}O$ records (Fig. 6l) (Cheng et al., 2016) and supported by multiple palaeorecords from the northern SCS (Fig. 6m) (Dai and Weng, 2015; Dai et al., 2015; Li et al., 2019; Luo et al., 2015; Sun et al., 2000a, b; Xie et al., 2014; Yu et al., 2017; Zhou et al., 2012). This strengthened monsoon brought increased moisture to the region, supporting the expansion of pine forests and ferns (Figs. 4 and 6j) and leading to a sharp reduction in fire activity, as evidenced by decreased charcoal concentrations (Fig. 6k).

Additional evidence supports this ecosystem-scale reorganization. Relatively high concentrations of foraminiferal organic linings (Fig. 4) indicate that water depth and open ocean environments had become suitable for planktonic foraminifera (Tyszka et al., 2021), while the decline in coprophilous fungal spores suggests an ecosystem-level re-

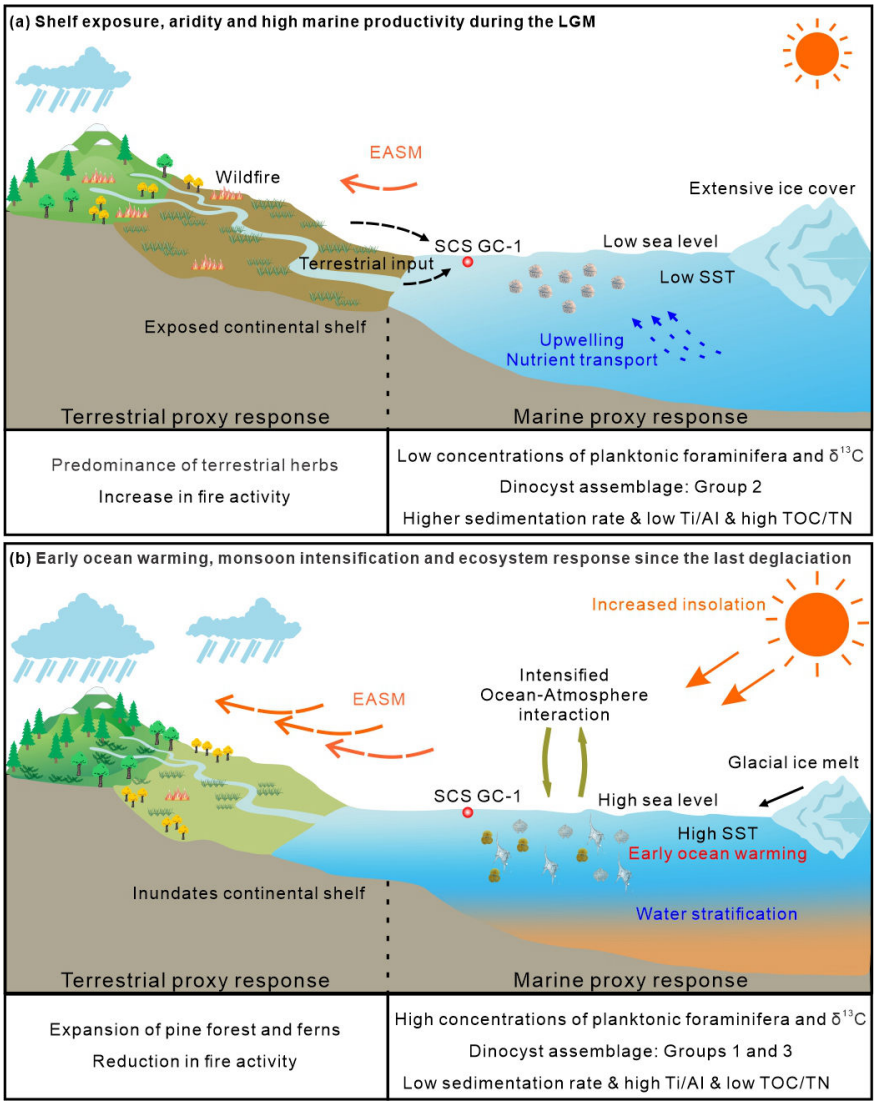

Figure 7. A conceptual framework of driving mechanisms and associated environmental responses during the LGM **(a)** and since the last deglaciation **(b)** based on multi-proxy record from the core SCS GC-1 in the northern SCS.

sponse in herbivore populations to the changing landscape (Fig. 4) (Lee et al., 2022). Similar patterns with increased fern spores, decreased terrestrial herbs and reduced dinocyst concentrations were also recorded from 12.5–6.8 ka in the core GLW31D from the northern SCS (Li et al., 2017). Additionally, periodic peaks in oligotrophic, open-ocean dinocyst Group 1, particularly around 10.6 and 5.8 ka (Fig. 6g), point to short enhancements of the warm, nutrient-poor Kuroshio Current intrusion (Liu et al., 2016b), which would further suppressed productivity in the northern SCS. Independent evidence for strengthened Kuroshio intrusion during the early Holocene is also recorded in core GLW31D from the northern SCS (Li et al., 2021).

Collectively, our multi-proxy dataset demonstrates that the deglacial environmental transition in the northern SCS reflects the complex interplay of multiple forcings (Fig. 7). The sequence began with tropical ocean warming, evidenced by the early rise in SST, which initiated the deglacial transition. This warming directly altered marine conditions (stratification, productivity) and, throughout ocean-atmospheric interactions, helped trigger the intensification of the EASM. These primary changes were then amplified and modulated by the physical effects of sea-level rise (altered sediment transport and coastal geography). This multi-mechanism framework highlights the northern SCS as a sensitive region where the coherent yet time-transgressive responses of marine and terrestrial systems to global climatic changes are clearly recorded during the last deglaciation.

6 Conclusions

Our multi-proxy reconstruction from the northern SCS provides a high-resolution record of clear glacial-interglacial climatic and oceanic transitions over the past 33 ka. Four distinct climatic phases are identified, viz. the pre-Last Glacial Maximum (32.8–27.3 ka), Last Glacial Maximum (27.3–17.0 ka), last deglaciation (including the Heinrich Stadial 1) (17.0–11.7 ka) and the Holocene (11.7 ka–present). The glacial intervals (pre-LGM and LGM) were characterized by higher sedimentation rates, cooler SST, higher primary productivity, herb-dominated landscapes, reduced humidity and intensified fire activity. This regime was primarily shaped by the effects of glacial low sea-level stand and arid climatic conditions, which together promoted the expansion of open vegetation and enhanced the supply of terrestrial nutrients, thereby stimulating marine productivity. A fundamental regime shift occurred during the last deglaciation, marked by evidently decreasing sedimentation rates, rising SST, declining primary productivity, a pronounced expansion of pine forests, increased moisture availability, and diminished fire activity. The early onset of SST warming (1.3 ka ahead of terrestrial shifts), points to tropical ocean-atmospheric interactions as the initial trigger for the deglacial transition. The Holocene was characterized by a period of relative stability, defined by the lowest sedimentation rates, warmest SST, highest humidity, maximum pine forest coverage and minimal fire disturbance. In summary, the combined evidence reveals that the environmental changes of the northern SCS since the last glacial period reflects a shift in the dominant climate forcing mechanisms. During the glacial period, the system was governed by the combined forcing of low sea level and continental aridity, which amplified land-sea interactions and maintained high marine productivity. Since the last deglaciation, the climate dynamics have transitioned to a regime where low-latitude processes, initiated by early ocean warming and subsequent ocean-atmosphere coupling, became the primary driver, leading to monsoon intensification and thereafter ecosystem reorganization. This study highlights the value of integrated land-sea proxies in deciphering complex climate interactions and underscores the northern SCS's sensitivity to both high- and low-latitude forcing. Future research employing a spatial network of cores across the SCS will be crucial to better resolve the spatial patterns and teleconnections of these changes.

Data availability. Data used in this study has been stored in the Pangaea database (https://www.pangaea.de) with specific DOI: https://doi.org/10.1594/PANGAEA.987882 (Zhao, 2026a) for pollen and spore, https://doi.pangaea.de/10.1594/PANGAEA.987861 (Zhao and Yao, 2026) for organic-walled dinoflagellate cyst, https://doi.org/10.1594/PANGAEA.987870 (Zhao, 2026b) for microcharcoal, https://doi.org/10.1594/PANGAEA.989845 (Zhao et al., 2026a) for organic carbon and nitrogen content, https://doi.org/10.1594/PANGAEA.989928 (Zhao et al., 2026b) for foraminifera stable carbon and oxygen isotopes, and https://doi.org/10.1594/PANGAEA.989846 (Zhao et al., 2026c) for X-ray fluorescence (XRF) scanning data.

Supplement. The supplement related to this article is available online at https://doi.org/10.5194/cp-22-1085-2026-supplement.

Author contributions. Xueqin Zhao: Conceptualization, Data curation, Formal analysis, Funding acquisition, Investigation, Methodology, Project administration, Supervision, Validation, Writing – original draft, Writing – review and editing; Shengjie Ye: Investigation, Visualization, Writing – review and editing; Jiahui Yao: Investigation, Formal analysis, Writing – review and editing; Michael Meadows: Validation, Writing – review and editing; Chengyu Weng: Validation, Writing – review and editing; Yasong Wang: Visualization, Writing – review and editing; Mingxing Zhang: Investigation; Yunping Xu: Conceptualization, Writing – review and editing.

Competing interests. The contact author has declared that none of the authors has any competing interests.

Disclaimer. Publisher's note: Copernicus Publications remains neutral with regard to jurisdictional claims made in the text, published maps, institutional affiliations, or any other geographical representation in this paper. The authors bear the ultimate responsibility for providing appropriate place names. Views expressed in the text are those of the authors and do not necessarily reflect the views of the publisher.

Acknowledgements. We would like to thank the captain, crew and especially all scientists of the R/V *Songhang* (Shanghai Ocean University) cruise for recovering the samples. Thank Xiaodi Lu and Yinwei Xi for the sampling and helping to measure XRF. Thank Xiaodi Lu for the assistance with lab analysis. We thank the three anonymous reviewers for their useful and constructive comments that have helped to improve the manuscript.

Financial support. This research has been supported by the National Natural Science Foundation of China, Youth Science Fund Project (grant no. 42206048).

Review statement. This paper was edited by Amaelle Landais and reviewed by three anonymous referees.

References

An, Z.: The history and variability of the East Asian paleomonsoon climate, Quat. Sci. Rev., 19, 171–187, https://doi.org/10.1016/S0277-3791(99)00060-8, 2000.

An, Z., Porter, S. C., Kutzbach, J. E., Xihao, W., Suming, W., Xiaodong, L., Xiaoqiang, L., and Weijian, Z.: Asynchronous Holocene optimum of the East Asian monsoon, Quat. Sci. Rev., 19, 743–762, https://doi.org/10.1016/S0277-3791(99)00031-1, 2000.

Bandara, G., Luo, C. X., Chen, C. X., Xiang, R., Herath, D. B., Yang, Z. J., and Thilakanayaka, V.: Sedimental pollen records in the northern South China Sea and their paleoenvironmental significance, J. Asian Earth Sci., 241, 105457, https://doi.org/10.1016/j.jseaes.2022.105457, 2023.

Barker, S., Greaves, M., and Elderfield, H.: A study of cleaning procedures used for foraminiferal Mg / Ca paleothermometry, Geochem. Geophys. Geosyst., 4, https://doi.org/10.1029/2003GC000559, 2003.

Blaauw, M. and Christen, J. A.: Flexible paleoclimate age-depth models using an autoregressive gamma process, Bayesian Anal., 6, 457–474, https://doi.org/10.1214/11-BA618, 2011.

Cartapanis, O., Bianchi, D., Jaccard, S. L., and Galbraith, E. D.: Global pulses of organic carbon burial in deep-sea sediments during glacial maxima, Nat. Commun., 7, 10796, https://doi.org/10.1038/ncomms10796, 2016.

Chao, S., Shaw, P., and Wang, J.: Wind relaxation as possible cause of the South China Sea Warm Current, J. Oceanogr., 51, 111–132, https://doi.org/10.1007/BF02235940, 1995.

Chen, C. A. and Huang, M.: A mid-depth front separating the South China Sea water and the Philippine sea water, J. Oceanogr., 52, 17–25, https://doi.org/10.1007/BF02236530, 1996.

Chen, Y., Huang, E., Schefuß, E., Mohtadi, M., Steinke, S., Liu, J., Martínez-Méndez, G., and Tian, J.: Wetland expansion on the continental shelf of the northern South China Sea during deglacial sea level rise, Quat. Sci. Rev., 231, 106202, https://doi.org/10.1016/j.quascirev.2020.106202, 2020.

Cheng, H., Edwards, R. L., Sinha, A., Spötl, C., Yi, L., Chen, S., Kelly, M., Kathayat, G., Wang, X., Li, X., Kong, X., Wang, Y., Ning, Y., and Zhang, H.: The Asian monsoon over the past 640 000 years and ice age terminations, Nature, 534, 640–646, https://doi.org/10.1038/nature18591, 2016.

Cheng, L., Abraham, J., Hausfather, Z., and Trenberth, K. E.: How fast are the oceans warming?, Science, 363, 128–129, https://doi.org/10.1126/science.aav7619, 2019.

Cheng, Z., Wu, J., Luo, C., Liu, Z., Huang, E., Zhao, H., Dai, L., and Weng, C.: Coexistence of savanna and rainforest on the ice-age Sunda Shelf revealed by pollen records from southern South China Sea, Quat. Sci. Rev., 301, 107947, https://doi.org/10.1016/j.quascirev.2022.107947, 2023.

Clark, P. U., Shakun, J. D., Baker, P. A., Bartlein, P. J., Brewer, S., Brook, E., Carlson, A. E., Cheng, H., Kaufman, D. S., Liu, Z., Marchitto, T. M., Mix, A. C., Morrill, C., Otto-Bliesner, B. L., Pahnke, K., Russell, J. M., Whitlock, C., Adkins, J. F., Blois, J. L., Clark, J., Colman, S. M., Curry, W. B., Flower, B. P., He, F., Johnson, T. C., Lynch-Stieglitz, J., Markgraf, V., McManus, J., Mitrovica, J. X., Moreno, P. I., and Williams, J. W.: Global climate evolution during the last deglaciation, P. Natl. Acad. Sci. USA, 109, E1134–E1142, https://doi.org/10.1073/pnas.1116619109, 2012.

Clift, P. D., Hodges, K. V., Heslop, D., Hannigan, R., Van Long, H., and Calves, G.: Correlation of Himalayan exhumation rates and Asian monsoon intensity, Nat. Geosci., 1, 875–880, https://doi.org/10.1038/ngeo351, 2008.

Conedera, M., Tinner, W., Neff, C., Meurer, M., Dickens, A. F., and Krebs, P.: Reconstructing past fire regimes: methods, applications, and relevance to fire management and conservation, Quat. Sci. Rev., 28, 555–576, https://doi.org/10.1016/j.quascirev.2008.11.005, 2009.

Dai, L. and Weng, C.: A survey on pollen dispersal in the western Pacific Ocean and its paleoclimatological significance as a proxy for variation of the Asian winter monsoon, Sci. China Earth Sci, 54, 249–258, https://doi.org/10.1007/s11430-010-4027-7, 2011.

Dai, L. and Weng, C.: Marine palynological record for tropical climate variations since the late last glacial maximum in the northern South China Sea, Deep-Sea. Res. Pt II, 122, 153–162, https://doi.org/10.1016/j.dsr2.2015.06.011, 2015.

Dai, L., Weng, C., and Mao, L.: Patterns of vegetation and climate change in the northern South China Sea during the last glaciation inferred from marine palynological records, Palaeogeogr. Palaeoclimatol. Palaeoecol., 440, 249–258, https://doi.org/10.1016/j.palaeo.2015.08.041, 2015.

Dale, B.: Dinoflagellate cyst ecology: modeling and geological applications, in: Palynology: principles and applications, edited by: Jansonius, J. and McGregor, D. C., American Association of Stratigraphic Palynologists Foundation, vol. 3, 1249–1275, ISBN 9780931871030, 1996.

Denton, G., Broecker, W., and Alley, R.: The mystery interval 17.5 to 14.5 kyrs ago, PAGES News, 14, 14–16, https://doi.org/10.22498/pages.14.2.14, 2006.

Ding, Z., Yu, Z., Rutter, N. W., and Liu, T.: Towards an orbital time scale for chinese loess deposits, Quat. Sci. Rev., 13, 39–70, https://doi.org/10.1016/0277-3791(94)90124-4, 1994.

Fang, G., Fang, W. D., and Wang, K.: A survey ofthe study of the South China Sea upper ocean circulation. Acta Oceanog. Tai., 37, 1–16, 1998.

Felden, J., Möller, L., Schindler, U., Huber, R., Schumacher, S., Koppe, R., Diepenbroek, M., and Glöckner, F. O.: PANGAEA – Data Publisher for Earth & Environmental Science, Sci. Data, 10, 347, https://doi.org/10.1038/s41597-023-02269-x, 2023.

Govin, A., Holzwarth, U., Heslop, D., Ford Keeling, L., Zabel, M., Mulitza, S., Collins, J. A., and Chiessi, C. M.: Distribution of major elements in Atlantic surface sediments (36° N–49° S): Imprint of terrigenous input and continental weathering, Geochem. Geophys. Geosyst., 13, https://doi.org/10.1029/2011GC003785, 2012.

Grimm, E.: Tilia and TGView 19 version 2.0. 41, software, Illinois State Museum, Research and Collection Center, Springfield, USA, https://www.neotomadb.org/apps/tilia (last access: 28 May 2026), 2015.

Hanebuth, T., Stattegger, K., and Grootes, P. M.: Rapid flooding of the Sunda Shelf: A late-glacial sea-level record, Science, 288, 1033–1035, https://doi.org/10.1126/science.288.5468.1033, 2000.

Haynes, J. R.: Foraminifera, Palgrave Macmillan London, https://doi.org/10.1007/978-1-349-05397-1, 1981.

Holzwarth, U., Esper, O., and Zonneveld, K.: Distribution of organic-walled dinoflagellate cysts in shelf surface sediments of the Benguela upwelling system in relationship to environmental conditions, Mar. Micropaleontol., 64, 91–119, https://doi.org/10.1016/j.marmicro.2007.04.001, 2007.

Hu, D., Clift, P. D., Böning, P., Hannigan, R., Hillier, S., Blusztajn, J., Wan, S., and Fuller, D. Q.: Holocene evolution in weathering and erosion patterns in the Pearl River delta, Geochem. Geophys. Geosyst., 14, 2349–2368, https://doi.org/10.1002/ggge.20166, 2013.

Hu, J., Kawamura, H., Hong, H., and Qi, Y.: A review on the currents in the South China Sea: Seasonal circulation, South China Sea warm current and Kuroshio intrusion, J. Oceanogr., 56, 607–624, https://doi.org/10.1023/A:1011117531252, 2000.

Huang, C., Wu, L., Cheng, J., Qu, X., Luo, Y., Zhang, H., Ye, F., and Wei, G.: Sedimentary responses to climatic variations and Kuroshio intrusion into the northern South China Sea since the last deglaciation, Global Planet. Change, 245, 104671, https://doi.org/10.1016/j.gloplacha.2024.104671, 2025.

Huang, K., You, C., Lin, H., and Shieh, Y.: In situ calibration of Mg / Ca ratio in planktonic foraminiferal shell using time series sediment trap: A case study of intense dissolution artifact in the South China Sea, Geochem. Geophys. Geosyst., 9, https://doi.org/10.1029/2007GC001660, 2008.

Hughen, K. A., Baillie, M. G. L., Bard, E., Warren Beck, J., Bertrand, C. J. H., Blackwell, P. G., Buck, C. E., Burr, G. S., Cutler, K. B., Damon, P. E., Edwards, R. L., Fairbanks, R. G., Friedrich, M., Guilderson, T. P., Kromer, B., McCormac, G., Manning, S., Bronk Ramsey, C., Reimer, P. J., Reimer, R. W., Remmele, S., Southon, J. R., Stuiver, M., Talamo, S., Taylor, F. W., Van der Plicht, J., and Weyhenmeyer, C. E.: Marine04 marine radiocarbon age calibration, 0–26 cal kyr BP, Radiocarbon, 46, 1059–1086, https://doi.org/10.1017/S0033822200033002, 2004.

Jiwarungrueangkul, T. and Liu, Z.: East Asian monsoon and sea-level controls on clay mineral variations in the southern South China Sea since the Last Glacial Maximum, Quat. Int., 592, 1–11, https://doi.org/10.1016/j.quaint.2021.04.033, 2021.

Kaars, S. V. D., Wang, X., Kershaw, P., Guichard, F., and Setiabudi, D. A.: A Late Quaternary palaeoecological record from the Banda Sea, Indonesia: patterns of vegetation, climate and biomass burning in Indonesia and northern Australia, Palaeogeogr. Palaeoclimatol. Palaeoecol., 155, 135–153, https://doi.org/10.1016/S0031-0182(99)00098-X, 2000.

Kissel, C., Laj, C., Jian, Z., Wang, P., Wandres, C., and Rebolledo-Vieyra, M.: Past environmental and circulation changes in the South China Sea: Input from the magnetic properties of deep-sea sediments, Quat. Sci. Rev., 236, 106263, https://doi.org/10.1016/j.quascirev.2020.106263, 2020.

Lambeck, K., Rouby, H., Purcell, A., Sun, Y., and Sambridge, M.: Sea level and global ice volumes from the Last Glacial Maximum to the Holocene, P. Natl. Acad. Sci. USA, 111, 15296–15303, https://doi.org/10.1073/pnas.1411762111, 2014.

Laskar, J., Robutel, P., Joutel, F., Gastineau, M., Correia, A. C. M., and Levrard, B.: A long-term numerical solution for the insolation quantities of the Earth, Astron. Astrophys., 428, 261–285, https://doi.org/10.1051/0004-6361:20041335, 2004.

Lee, C. M., van Geel, B., and Gosling, W. D.: On the use of spores of coprophilous fungi preserved in sediments to indicate past herbivore presence, Quaternary, 5, 30, https://doi.org/10.3390/quat5030030, 2022.

Li, C., Li, Y., Zheng, Y., Yu, S., Tang, L., Li, B., and Cui, Q.: A high-resolution pollen record from East China reveals large climate variability near the Northgrippian-Meghalayan boundary (around 42 years ago) exerted societal influence, Palaeogeogr. Palaeoclimatol. Palaeoecol., 512, 156–165, https://doi.org/10.1016/j.palaeo.2018.07.031, 2018a.

Li, M., Ouyang, T., Tian, C., Zhu, Z., Peng, S., Tang, Z., Qiu, Y., Zhong, H., and Peng, X.: Sedimentary responses to the East Asian monsoon and sea level variations recorded in the northern South China Sea over the past 3 kyr, J. Asian Earth Sci., 171, 213–224, https://doi.org/10.1016/j.jseaes.2018.01.001, 2019.

Li, Z., Pospelova, V., Liu, L., Zhou, R., and Song, B.: High-resolution palynological record of Holocene climatic and oceanographic changes in the northern South China Sea, Palaeogeogr. Palaeoclimatol. Palaeoecol., 483, 94–124, https://doi.org/10.1016/j.palaeo.2017.03.009, 2017.

Li, Z., Pospelova, V., Lin, H.-L., Liu, L., Song, B., and Gong, W.: Seasonal dinoflagellate cyst production and terrestrial palynomorph deposition in the East Asian Monsoon influenced South China Sea: A sediment trap study from the Southwest Taiwan waters, Rev. Palaeobot. Palynol., 257, 117–139, https://doi.org/10.1016/j.revpalbo.2018.07.007, 2018b.

Li, Z., Pospelova, V., Kawamura, H., Luo, C., Mertens, K. N., Hernández-Almeida, I., Yin, K., Wu, Y., Wu, H., and Xiang, R.: Dinoflagellate cyst distribution in surface sediments from the South China Sea in relation to hydrographic conditions and primary productivity, Mar. Micropaleontol., 159, 101815, https://doi.org/10.1016/j.marmicro.2019.101815, 2020.

Li, Z., Pospelova, V., Liu, L., Francois, R., Wu, Y., Mertens, K. N., Saito, Y., Zhou, R., Song, B., and Xie, X.: High-resolution reconstructions of Holocene sea-surface conditions from dinoflagellate cyst assemblages in the northern South China Sea, Mar. Geol., 438, 106528, https://doi.org/10.1016/j.margeo.2021.106528, 2021.

Li, Z., Pospelova, V., Mertens, K. N., Liu, L., Wu, Y., Li, C., and Gu, H.: Evaluation of organic-walled dinoflagellate cyst distributions in coastal surface sediments of the China Seas in relation with hydrographic conditions for paleoceanographic reconstruction, Quat. Int., 661, 60–75, https://doi.org/10.1016/j.quaint.2023.03.007, 2023.

Lin, D., Chen, M., Yamamoto, M., and Yokoyama, Y.: Millennial-scale alkenone sea surface temperature changes in the northern South China Sea during the past 45 000 years (MD972146), Quat. Int., 333, 207–215, https://doi.org/10.1016/j.quaint.2014.03.062, 2014.

Liu, J., Xiang, R., Chen, Z., Chen, M., Yan, W., Zhang, L., and Chen, H.: Sources, transport and deposition of surface sediments from the South China Sea, Deep-Sea Res. Pt. I, 71, 92–102, https://doi.org/10.1016/j.dsr.2012.09.006, 2013.

Liu, J., Xiang, R., Kao, S. J., Fu, S., and Zhou, L.: Sedimentary responses to sea-level rise and Kuroshio Current intrusion since the Last Glacial Maximum: Grain size and clay mineral evidence from the northern South China Sea slope, Palaeogeogr. Palaeoclimatol. Palaeoecol., 450, 111–121, https://doi.org/10.1016/j.palaeo.2016.03.002, 2016a.

Liu, K., Chao, S., Shaw, P., Gong, G., Chen, C., and Tang, T.: Monsoon-forced chlorophyll distribution and pri-

mary production in the South China Sea: observations and a numerical study, Deep-Sea Res. Pt. I, 49, 1387–1412, https://doi.org/10.1016/S0967-0637(02)00035-3, 2002.

Liu, L., Guan, H., Feng, J., Xu, L., Mao, S., and Liu, L.: Composition of glycerol dibiphytanyl glycerol tetraethers (GDGTs) and its responses to paleotemperature and monsoon changes since 31 ka in northern South China Sea, Mar. Geol. & Qua. Geol., 40, 144–159, https://doi.org/10.16562/j.cnki.0256-1492.2020021101, 2020.

Liu, Z., Trentesaux, A., Clemens, S. C., Colin, C., Wang, P., Huang, B., and Boulay, S.: Clay mineral assemblages in the northern South China Sea: implications for East Asian monsoon evolution over the past 2 million years, Mar. Geol., 201, 133–146, https://doi.org/10.1016/S0025-3227(03)00213-5, 2003.

Liu, Z., Colin, C., Li, X., Zhao, Y., Tuo, S., Chen, Z., Siringan, F. P., Liu, J. T., Huang, C.-Y., You, C.-F., and Huang, K.-F.: Clay mineral distribution in surface sediments of the northeastern South China Sea and surrounding fluvial drainage basins: Source and transport, Mar. Geol., 277, 48–60, https://doi.org/10.1016/j.margeo.2010.08.010, 2010.

Liu, Z., Zhao, Y., Colin, C., Stattegger, K., Wiesner, M. G., Huh, C., Zhang, Y., Li, X., Sompongchaiyakul, P., You, C., Huang, C., Liu, J. T., Siringan, F. P., Le, K. P., Sathiamurthy, E., Hantoro, W. S., Liu, J., Tuo, S., Zhao, S., Zhou, S., He, Z., Wang, Y., Bunsomboonsakul, S., and Li, Y.: Source-to-sink transport processes of fluvial sediments in the South China Sea, Earth-Sci. Rev., 153, 238–273, https://doi.org/10.1016/j.earscirev.2015.08.005, 2016b.

Luo, C., Chen, M., Xiang, R., Liu, J., Zhang, L., and Lu, J.: Comparison of modern pollen distribution between the northern and southern parts of the South China Sea, Int. J. Biometeorol., 59, 397–415, https://doi.org/10.1007/s00484-014-0852-2, 2015.

Luo, C., Jiang, C., Yang, M., Chen, M., Xiang, R., Zhang, L., Liu, J., and Pan, A.: Transportation modes of pollen in surface waters in the South China Sea and their environmental significance, Rev. Palaeobot. Palynol., 225, 95–105, https://doi.org/10.1016/j.revpalbo.2015.11.004, 2016.

Luo, C., Chen, C., Xiang, R., Jiang, W., Liu, J., Lu, J., Su, X., Zhang, Q., Yang, Y., and Yang, M.: Study of modern pollen distribution in the northeastern Indian Ocean and their application to paleoenvironment reconstruction, Rev. Palaeobot. Palynol., 256, 50–62, https://doi.org/10.1016/j.revpalbo.2018.05.007, 2018.

Luo, Y. and Sun, X.: Vegetation evolution and millennial-scale climatic fluctuations since Last Glacial Maximum in pollen record from northern South China Sea, Chin. Sci. Bull., 50, 793–799, https://doi.org/10.1007/BF03183681, 2005.

Luo, Y. and Sun, X.: Vegetation evolution and its response to climatic change during 3.15–0.67 Ma in deep-sea pollen record from northern South China Sea, Chin. Sci. Bull., 58, 364–372, https://doi.org/10.1007/s11434-012-5374-x, 2013.

Maher, L. J.: Nomograms for computing 0.95 confidence limits of pollen data, Rev. Palaeobot. Palynol., 13, 85–93, https://doi.org/10.1016/0034-6667(72)90038-3, 1972.

Marret, F. and Zonneveld, K. A. F.: Atlas of modern organic-walled dinoflagellate cyst distribution, Rev. Palaeobot. Palynol., 125, 1–200, https://doi.org/10.1016/S0034-6667(02)00229-4, 2003.

Matsuoka, K.: Dinoflagellate cysts and pollen in pelagic sediments of the northern part of the Philippin Sea, Bull. Faculty of Liberal Arts, Nagasaki University (Natural Science), 21, 59–70, https://fileserver-az.core.ac.uk/download/483769045.pdf (last access: 28 May 2026), 1981.

Meyers, P. A.: Organic geochemical proxies of paleoceanographic, paleolimnologic, and paleoclimatic processes. Org. Geochem., 27, 213–250, https://doi.org/10.1016/S0146-6380(97)00049-1, 1997.

Milliman, J. D. and Syvitski, J. P. M.: Geomorphic/tectonic control of sediment discharge to the ocean: The importance of small mountainous rivers, J. Geol., 100, 525–544, https://doi.org/10.1086/629606, 1992.

Mooney, S. D. and Tinner, W.: The analysis of charcoal in peat and organic sediments, Mires Peat, 7, https://doi.org/10.19189/001c.128417, 2011.

North Greenland Ice Core Project members: High-resolution record of Northern Hemisphere climate extending into the last interglacial period, Nature, 431, 147–151, https://doi.org/10.1038/nature02805, 2004.

Oppo, D. W. and Sun, Y.: Amplitude and timing of sea-surface temperature change in the northern South China Sea: Dynamic link to the East Asian monsoon, Geology, 33, 785–788, https://doi.org/10.1130/G21867.1, 2005.

Reagan, J. R., Garcia, H. E., Boyer, T. P., Baranova, O. K., Bouchard, C., Cross, S. L., Dukhovskoy, D., Grodsky, A. I., Locarnini, R. A., Mishonov, A. V., Paver, C. R., Seidov, D., and Wang, Z.: World Ocean Atlas 2023: Product Documentation, edited by: Mishonov, A., https://doi.org/10.25923/a78k-gq49, 2023.

Sanchez Goñi, M. F. and Harrison, S. P.: Millennial-scale climate variability and vegetation changes during the Last Glacial: Concepts and terminology, Quat. Sci. Rev., 29, 2823–2827, https://doi.org/10.1016/j.quascirev.2009.11.014, 2010.

Schönfeld, J., Alve, E., Geslin, E., Jorissen, F., Korsun, S., and Spezzaferri, S.: The FOBIMO (FOraminiferal BIo-MOnitoring) initiative – Towards a standardised protocol for soft-bottom benthic foraminiferal monitoring studies, Mar. Micropaleontol., 94–95, 1–13, https://doi.org/10.1016/j.marmicro.2012.06.001, 2012.

Smayda, T. J. and Trainer, V. L.: Dinoflagellate blooms in upwelling systems: Seeding, variability, and contrasts with diatom bloom behaviour, Prog. Oceanogr., 85, 92–107, https://doi.org/10.1016/j.pocean.2010.02.006, 2010.

Stibig, H.-J., Belward, A. S., Roy, P. S., Rosalina-Wasrin, U., Agrawal, S., Joshi, P. K., Beuchle, R., Fritz, S., Mubareka, S., and Giri, C.: A land-cover map for South and Southeast Asia derived from SPOT-VEGETATION data, J. Biogeogr., 34, 625–637, https://doi.org/10.1111/j.1365-2699.2006.01637.x, 2007.

Stuiver, M. and Reimer, P. J.: Extended 14C Data Base and Revised CALIB 3.0 14C Age Calibration Program, Radiocarbon, 35, 215–230, https://doi.org/10.1017/S0033822200013904, 1993.

Sun, X. and Luo, Y.: Pollen record of the last 280 ka from deep sea sediments of the northern South China Sea, Sci. China Ser. D-Earth Sci., 44, 879–888, https://doi.org/10.1007/BF02907079, 2001.

Sun, X., Li, X., and Beug, H.-J.: Pollen distribution in hemipelagic surface sediments of the South China Sea and its relation to modern vegetation distribution, Mar. Geol., 156, 211–226, https://doi.org/10.1016/S0025-3227(98)00180-7, 1999.

Sun, X., Li, X., and Chen, H.: Evidence for natural fire and climate history since 37 ka BP in the northern part of the

South China Sea, Sci. China Ser. D-Earth Sci., 43, 487–493, https://doi.org/10.1007/bf02875310, 2000a.

Sun, X., Li, X., Luo, Y., and Chen, X.: The vegetation and climate at the last glaciation on the emerged continental shelf of the South China Sea, Palaeogeogr. Palaeoclimatol. Palaeoecol., 160, 301–316, https://doi.org/10.1016/S0031-0182(00)00078-X, 2000b.

Sun, X., Luo, Y., Huang, F., Tian, J., and Wang, P.: Deep-sea pollen from the South China Sea: Pleistocene indicators of East Asian monsoon, Mar. Geol., 201, 97–118, https://doi.org/10.1016/S0025-3227(03)00211-1, 2003.

Tang, L., Mao, L., Shu, J., Li, C., Shen, C., and Zhou, Z.: Atlas of Quaternary pollen and spores in China. Science Press and Springer Nature Singapore Pte Ltd, https://doi.org/10.1007/978-981-13-7103-5, 2020.

ter Braak, C. J. F. and Smilauer, P.: Canoco reference manual and user's guide: software for ordination, version 5.0. Microcomputer Power, Ithaca, NY, USA, https://www.canoco5.com (last access: 28 May 2026), 2012.

Tian, J., Wang, P. X., and Cheng, X. R.: Responses of foraminiferal isotopic variations at ODP Site 1143 in the southern South China Sea to orbital forcing, Sci. China Ser. D-Earth Sci., 47, 943–953, https://doi.org/10.1360/03yd0129, 2004.

Tian, J., Huang, E., and Pak, D. K.: East Asian winter monsoon variability over the last glacial cycle: Insights from a latitudinal sea-surface temperature gradient across the South China Sea, Palaeogeogr. Palaeoclimatol. Palaeoecol., 292, 319–324, https://doi.org/10.1016/j.palaeo.2010.04.005, 2010.

Tian, J., Xie, X., Ma, W., Jin, H., and Wang, P.: X-ray fluorescence core scanning records of chemical weathering and monsoon evolution over the past 5 Myr in the southern South China Sea, Paleoceanography, 26, https://doi.org/10.1029/2010PA002045, 2011.

Tyszka, J., Godos, K., Goleń, J., and Radmacher, W.: Foraminiferal organic linings: Functional and phylogenetic challenges, Earth-Sci. Rev., 220, 103726, https://doi.org/10.1016/j.earscirev.2021.103726, 2021.

Wan, S. and Jian, Z.: Deep water exchanges between the South China Sea and the Pacific since the last glacial period, Paleoceanography, 29, 1162–1178, https://doi.org/10.1002/2013PA002578, 2014.

Wan, S., Li, A., Clift, P. D., and Stuut, J.-B. W.: Development of the East Asian monsoon: Mineralogical and sedimentologic records in the northern South China Sea since 20 Ma, Palaeogeogr. Palaeoclimatol. Palaeoecol., 254, 561–582, https://doi.org/10.1016/j.palaeo.2007.07.009, 2007.

Wang, C.: The forests of China. Maria Moors Cabot Foundation No. 5, Harvard University, Cambridge Mass, USA, 717 pp., https://catalog.libraries.psu.edu/catalog/781778 (last access: 28 May 2026), 1961.

Wang, L., Sarnthein, M., Erlenkeuser, H., Grootes, P. M., Grimalt, J. O., Pelejero, C., and Linck, G.: Holocene variations in Asian monsoon moisture: A bidecadal sediment record from the South China Sea, Geophys. Res. Lett., 26, 2889–2892, https://doi.org/10.1029/1999GL900443, 1999.

Wang, P. and Sun, X.: Last glacial maximum in China: comparison between land and sea, Catena, 23, 341–353, https://doi.org/10.1016/0341-8162(94)90077-9, 1994.

Wang, P., Li, Q., and Tian, J.: Pleistocene paleoceanography of the South China Sea: Progress over the past 20 years, Mar. Geol., 352, 381–396, https://doi.org/10.1016/j.margeo.2014.03.003, 2014.

Wang, P., Wang, B., Cheng, H., Fasullo, J., Guo, Z., Kiefer, T., and Liu, Z.: The global monsoon across time scales: Mechanisms and outstanding issues, Earth-Sci. Rev., 174, 84–121, https://doi.org/10.1016/j.earscirev.2017.07.006, 2017.

Wang, X., Sun, X., Wang, P., and Stattegger, K.: Vegetation on the Sunda Shelf, South China Sea, during the Last Glacial Maximum, Palaeogeogr. Palaeoclimatol. Palaeoecol., 278, 88–97, https://doi.org/10.1016/j.palaeo.2009.04.008, 2009.

Wang, Y. J., Cheng, H., Edwards, R. L., An, Z. S., Wu, J. Y., Shen, C.-C., and Dorale, J. A.: A high-resolution absolute-dated late Pleistocene monsoon record from Hulu Cave, China, Science, 294, 2345–2348, https://doi.org/10.1126/science.1064618, 2001.

Wei, G., Liu, Y., Li, X., Shao, L., and Fang, D.: Major and trace element variations of the sediments at ODP Site 1144, South China Sea, during the last 230 ka and their paleoclimate implications, Palaeogeogr. Palaeoclimatol. Palaeoecol., 212, 331–342, https://doi.org/10.1016/j.palaeo.2004.06.011, 2004.

Whitmore, T. C.: Rain forests: Tropical rain forests of the far east, Science, 228, 874-,875, https://doi.org/10.1126/science.228.4701.874, 1985.

Williams, G. L., Fensome, R. A., and MacRae, R. A.: The Lentin and Williams index of fossil dinoflagellates 2017 edition. AASP Contributions Series, 48, https://palynology.org/wp-content/uploads/2017/01/AASP-Contribution-Series-No.48.pdf (last access: 28 May 2026), 2017.

Xie, S.-P., Deser, C., Vecchi, G. A., Ma, J., Teng, H., and Wittenberg, A. T.: Global Warming Pattern Formation: Sea Surface Temperature and Rainfall, J. Clim., 23, 966–986, https://doi.org/10.1175/2009JCLI3329.1, 2010.

Xie, X., Zheng, H.-B., and Qiao, P.-J.: Millennial climate changes since MIS 3 revealed by element records in deep-sea sediments from northern South China Sea, Chin. Sci. Bull., 59, 776–784, https://doi.org/10.1007/s11434-014-0117-9, 2014.

Xu, D., Lu, H., Wu, N., Liu, Z., Li, T., Shen, C., and Wang, L.: Asynchronous marine-terrestrial signals of the last deglacial warming in East Asia associated with low- and high-latitude climate changes, P. Natl. Acad. Sci. USA, 110, 9657–9662, https://doi.org/10.1073/pnas.1300025110, 2013.

Xu, Y., Li, B.-H., and Cui, Q.: Orbital forcing on paleoproductivity in the northern South China sea during the late Pleistocene, Quat. Sci. Rev., 350, 109170, https://doi.org/10.1016/j.quascirev.2024.109170, 2025.

Yu, S., Zheng, Z., Chen, F., Jing, X., Kershaw, P., Moss, P., Peng, X., Zhang, X., Chen, C., Zhou, Y., Huang, K., and Gan, H.: A last glacial and deglacial pollen record from the northern South China Sea: New insight into coastal-shelf paleoenvironment, Quat. Sci. Rev., 157, 114–128, https://doi.org/10.1016/j.quascirev.2016.12.012, 2017.

Yuan, Y. C., Bu, X. W., Liao, G. H., Lou, R. Y., Su, J. L., and Wang, K. S.: Diagnostic calculation of the upper-layer circulation in the South China Sea during the winter of 1998, Acta Oceanol. Sin., 23, 187–199, 2004.

Zanzarini, V., Andersen, A. N., and Fidelis, A.: Flammability in tropical savannas: Variation among growth forms and seasons in Cerrado, Biotropica, 54, 979–987, https://doi.org/10.1111/btp.13121, 2022.

Zhang, H., Liu, C., Jin, X., Shi, J., Zhao, S., and Jian, Z.: Dynamics of primary productivity in the northern South China Sea over the past 24 000 years, Geochem. Geophys. Geosyst., 17, 4878–4891, https://doi.org/10.1002/2016GC006602, 2016.

Zhao, X.: Pollen analysis of marine sediment core SCS_GC-1, PANGAEA [data set], https://doi.org/10.1594/PANGAEA.987882, 2026a.

Zhao, X.: Microcharcoal data of marine sediment core SCS_GC-1, PANGAEA [data set], https://doi.org/10.1594/PANGAEA.987870, 2026b.

Zhao, X. and Yao, J.: Organic-walled dinoflagellate cyst data of marine sediment core SCS_GC-1, PANGAEA [data set], https://doi.org/10.1594/PANGAEA.987861, 2026.

Zhao, X., Dupont, L., Schefuß, E., Bouimetarhan, I., and Wefer, G.: Palynological evidence for Holocene climatic and oceanographic changes off western South Africa, Quat. Sci. Rev., 165, 88–101, https://doi.org/10.1016/j.quascirev.2017.04.022, 2017.

Zhao, X., Ye, S., Yao, J., Meadows, M. E., Weng, C., Wang, Y., Zhang, M., and Xu, Y.: Carbon and nitrogen content of marine sediment core SCS GC-1, PANGAEA [data set], https://doi.org/10.1594/PANGAEA.989845, 2026a.

Zhao, X., Ye, S., Yao, J., Meadows, M. E., Weng, C., Wang, Y., Zhang, M., and Xu, Y.: Foraminifera stable isotopes of marine sediment core SCS GC-1, PANGAEA [data set], https://doi.org/10.1594/PANGAEA.989928, 2026b.

Zhao, X., Ye, S., Yao, J., Meadows, M. E., Weng, C., Wang, Y., Zhang, M., and Xu, Y.: X-ray fluorescence (XRF) scanning of marine sediment core SCS GC-1, PANGAEA [data set], https://doi.org/10.1594/PANGAEA.989846, 2026c.

Zheng, Z. and Lei, Z. Q.: A 400 000 year record of vegetational and climatic changes from a volcanic basin, Leizhou Peninsula, southern China, Palaeogeogr. Palaeoclimatol. Palaeoecol., 145, 339–362, https://doi.org/10.1016/S0031-0182(98)00107-2, 1999.

Zhong, Y., Chen, Z., Li, L., Liu, J., Li, G., Zheng, X., Wang, S., and Mo, A.: Bottom water hydrodynamic provinces and transport patterns of the northern South China Sea: Evidence from grain size of the terrigenous sediments, Cont. Shelf Res., 140, 11–26, https://doi.org/10.1016/j.csr.2017.01.023, 2017.

Zhou, B., Zheng, H., Yang, W., Taylor, D., Lu, Y., Wei, G., Li, L., and Wang, H.: Climate and vegetation variations since the LGM recorded by biomarkers from a sediment core in the northern South China Sea, J. Quat. Sci., 27, 948–955, https://doi.org/10.1002/jqs.2588, 2012.

Zonneveld, K. A. F. and Pospelova, V.: A determination key for modern dinoflagellate cysts, Palynology, 39, 387–409, https://doi.org/10.1080/01916122.2014.990115, 2015.

Zonneveld, K. A. F., Versteegh, G., and Kodrans-Nsiah, M.: Preservation and organic chemistry of Late Cenozoic organic-walled dinoflagellate cysts: A review, Mar. Micropaleontol., 68, 179–197, https://doi.org/10.1016/j.marmicro.2008.01.015, 2008.

Zonneveld, K. A. F., Marret, F., Versteegh, G. J. M., Bogus, K., Bonnet, S., Bouimetarhan, I., Crouch, E., de Vernal, A., Elshanawany, R., Edwards, L., Esper, O., Forke, S., Grøsfjeld, K., Henry, M., Holzwarth, U., Kielt, J. F., Kim, S., Ladouceur, S., Ledu, D., Chen, L., Limoges, A., Londeix, L., Lu, S. H., Mahmoud, M. S., Marino, G., Matsouka, K., Matthiessen, J., Mildenhal, D. C., Mudie, P., Neil, H. L., Pospelova, V., Qi, Y., Radi, T., Richerol, T., Rochon, A., Sangiorgi, F., Solignac, S., Turon, J. L., Verleye, T., Wang, Y., Wang, Z., and Young, M.: Atlas of modern dinoflagellate cyst distribution based on 2405 data points, Rev. Palaeobot. Palynol., 191, 1–197, https://doi.org/10.1016/j.revpalbo.2012.08.003, 2013.

Zonneveld, K. A. F., Harper, K., Klügel, A., Chen, L., De Lange, G., and Versteegh, G. J. M.: Climate change, society, and pandemic disease in Roman Italy between 200 BCE and 600 CE, Sci. Adv., 10, eadk1033, https://doi.org/10.1126/sciadv.adk1033, 2024.